Interaction between Galaxies and the Intergalactic Medium at $z = 3$

TUMMUANGPAK, PIMPUNYAWAT

Interaction between Galaxies and the Intergalactic Medium at z = 3

Pimpunyawat Tummuangpak

A thesis submitted to the University of Durham
in accordance with the regulations for
admittance to MSc. by Research.

November 2009

Department of Physics
University of Durham

Abstract

In this thesis, we aim to study the clustering properties of galaxies at z $\approx$ 3 and the relationship between galaxies and the IGM at these redshift via clustering correlation functions. We use the combined data from the VLT LBG Survey (Bielby, 2008) and the Keck survey (Steidel, 2003) to measure the LBG-LBG correlation function. We aim to estimate the infall parameter, β from the ratio of LBG-LBG correlation function in redshift space, $\xi(s)$, and in real space, $\xi(r)$. We found agreement with Bielby et al. (2008) in the $\xi(s)$ result from the VLT data. Our LBG-LBG $\xi(s)$ from the combined data is consistent with the observed $\xi(s)$ from da Angela et al. (2005), where $\gamma = 1.71$ and $s_0 = 5.1$ h^{-1} Mpc. We also tested the effect of redshift errors by using the $z-$space distortions model from da Angela et al. (2005) with our parameters. We found the peculiar velocities had a smaller effect in the combined data compared to only VLT data. This may be because smaller redshift errors in Steidel et al. (2003). By computing and fitting $\xi(s)/\xi(r)$, we get $\beta = 0.14^{+0.09}_{-0.05}$ at $z = 3$. This gives a bias factor, $b = 6.8$. This result agrees with Bielby et al. (2008), $\beta = 0.21^{+0.13}_{-0.12}$, estimated by fitting the power-law $\xi(r)$ to the measurement of $\xi(\sigma, \pi)$ from the combined data.

We then calculate the Lyα-LBG and LBG-CIV correlation function. We attempt to (a) investigate the effect of feedback on the LBG-Lyα cross correlation, (b) compare the LBG-CIV cross-correlation with LBG-LBG $\xi(s)$ to see if CIV absorption systems are distributed like LBGs. We use a different approach to reanalyze the Lyα-LBG $\xi(s)$, with different ways of estimating the error to compare our result with Bielby et al. (2008). Our results agree with those of Bielby et al. (2008) but with slightly smaller error bars. Results from high and low resolution QSO spectra are compared to the results of Adelberger et al. (2003) and Adelberger et al. (2005). We found a decrease in transmissivity at distances below $3h^{-1}$ Mpc and an increase of $< flux/cont >$ to the mean value at larger scales.

We detected how these results were affected by the LBG velocity dispersion found in Chapter 3. We also perform CIV-LBG cross correlation. It is consistent with the LBG-LBG auto-correlation function. This is consistent with CIV systems and LBGs being the same objects as they show the same clustering behaviour.

We then employed the GIMIC simulations to create synthetic Lyα spectra and Galaxies. Our main aims are to study (a) the LBG-LBG $\xi(s)$ to see if we can detect the effects of peculiar velocities by comparing real and redshift space correlation functions, (b) the LBG-Lyα $\xi(s)$ to understand more about outflow and feedback. We selected galaxies in the simulation by stellar mass. From our results, the LBG-LBG correlation functions in real and redshift space tend to appear as power laws. The effect of peculiar velocities in redshift space has been detected since the LBG-LBG $\xi(s)$ in redshift space tends to have lower clustering than $\xi(r)$ in real space at small scales. From the LBG-Lyα $\xi(s)$, we found a decrease in $< flux/cont >$ at separations below 5 h^{-1} Mpc. $\xi(s)$ increases and reaches the mean value at $< flux/cont > \approx 0.70$ at larger scales. At small distances near LBGs, we see no effect from the wind from the simulations. The results seem to agree with Adelberger et al. (2005) rather than Adelberger et al. (2003). Therefore they are less in agreement with our VLT results which show some evidence for feedback at small scales.

Contents

List of Tables

List of Figures

Declaration

This thesis was undertaken between 2008 and 2009 while the author was a research student under the supervision of Professor Tom Shanks in the Department of Physics at the University of Durham. This work has not been submitted for any other degree at the University of Durham or any other University.

Acknowledgements

Firstly, I would like to give my deepest thanks to my supervisor Professor Tom Shanks who always guide, understand and be patient with me. Also I would like to give many thanks to people in Durham who always help and inspire me. Thank to Dr. N. Crighton for the simulations things and many guidances, Utane Sawangwit who always guide me many things about my works and life in Durham. Thanks Julie and Andy, my lovely officemates who always help me. Thank to my Thai friends here, without you guys my life will be more difficult. I acknowledge the funding from Thai Government Scholarship. Last but not least, I wish to thank my family who always love and support me.

Chapter 1

Introduction to Cosmology and Galaxy Clustering

In order to pursue the main investigations of this thesis, we need to understand the model that is used to explain the universe. The cosmological principle is the theoretical assumption that underpins modern cosmological models. From the cosmological principle, our universe is assumed to be isotropic and homogeneous on the large-scale. Isotropic means the universe looks the same in all directions, while homogeneous means the universe looks the same at each point. From these assumptions, the basic details of the standard cosmology are presented as follows.

1.1 Ingredients of the standard cosmology

1.1.1 The expanding Universe

Observations show that most galaxies are moving away from us. Hubble's law gives locally $v = H_0 d$ where v is the recession velocity of a galaxy at distance d and H_0 is Hubble's constant. For small v, the redshift parameter, z is used to parameterise velocity, where $z = \frac{v}{c}$. This is because to first order the redshift can be explained as a Doppler effect with $\lambda_{obs} = (1 + v/c)\lambda_{em} = (1 + z)\lambda_{em}$. Here λ_{obs} is the wavelength of an absorption or emission line redshifted from the the emission wavelength λ_{em}. So to first order $d = \frac{cz}{H_0}$. More generally, redshift is related to the scale factor or expansion factor as

$$1 + z = \frac{\lambda_{obs}}{\lambda_{em}} = \frac{a_0}{a(t)} \tag{1.1}$$

where the the subscript zero referes to the present time.

The expansion factor $a(t)$ can then be written in terms of a comoving coordinate $\bar{x}$ and a physical coordinate as

$$\bar{r} = \frac{a_0}{a(t)}\bar{x} \tag{1.2}$$

The Robertson-Walker metric is established through the modern cosmology assumption that our universe is isotropic and homogeneous on the large-scale. It is defined as follows:

$$ds^2 = -dt^2 + a(t)^2(\frac{dr^2}{1-kr^2} + r^2(d\theta^2 + sin^2\theta d\phi^2)) \tag{1.3}$$

Throughout we assume units where the speed of light c =1. $\hbar$ is also assumed to be unity. The curvature parameter k can be +1, 0, -1 for positive curvature (closed universe), flat universe, and negative curvature (open universe) respectively. $a(t)$ represents the expansion factor. By applying the Robertson-Walker solution to Einstein's equations, it is reduced to Friedmann's equations which can be used to explain the expansion of the universe.

$$H^2 = (\frac{\dot{a}}{a})^2 = \frac{8\pi G}{3}\rho - \frac{k}{a^2} \tag{1.4}$$

and

$$\frac{\ddot{a}}{a} = -\frac{4\pi G}{3}(\rho + 3p) \tag{1.5}$$

where H is the Hubble constant $H = \frac{\dot{a}}{a}$, ρ is the overall energy-mass density and p is the isotropic pressure in its rest frame. G is the gravitational constant.

1.1.2 Cosmological parameters

The density parameter Ω_0

The density of the universe can be specified by the density parameter. From Friedmann's equations, the critical value of the energy density in the flat geometry (k=0) is:

$$\rho_{crit}(t) = \frac{3H^2}{8\pi G} \tag{1.6}$$

The critical density is time-dependent. H_0 is 100 h km s^{-1} Mpc^{-1} where $h = 0.72 \pm 0.08$. Since $G = 6.67 \times 10^{-11} m^3$ kg^{-1} sec^{-2}, then

$$\begin{aligned} \rho_{crit}(t_0) &= 1.88h^2 \times 10^{-26} kgm^{-3} \\ &= 2.78h^{-1} \times 10^{11} M_\odot/(h^{-1}Mpc)^3 \end{aligned} \tag{1.7}$$

The critical density is not the real universal density but it is set to be a scale for the universal density. Furthermore, it is easier to express the true density of the universe, ρ, to the critical density, called **the density parameter** Ω.

$$\Omega(t) = \frac{\rho}{\rho_{crit}} \tag{1.8}$$

The Friedmann equations are now expressed in term of density parameter.

$$H^2 = \frac{8\pi G}{3}\rho - \frac{k}{a^2} = \frac{8\pi G}{3}\rho_{crit}\Omega - \frac{k}{a^2} = H^2\Omega - \frac{k}{a^2} \tag{1.9}$$

Then

$$\Omega - 1 = \frac{k}{a^2H^2} \tag{1.10}$$

When $k = 0$, $\Omega = 1$. In this case, it is often called a critical-density Universe. This implies the true independent type of the matter that we have in the universe (Liddle, 2007). However, when $\Omega \neq 1$, Friedmann's equation is very useful for analyzing the evolution of the density. There are many different types of matter which can be expressed by the different notation of the density component, for instance, Ω_{mat} , Ω_{rad}. The density parameter can also be expressed in term of the curvature, k,

$$\Omega_k = -\frac{k}{a^2H^2} \tag{1.11}$$

$$\Omega + \Omega_k = 1 \tag{1.12}$$

1.1.3 The cosmological constant

Einstein proposed a modification parameter to apply in a static universe. Λ is set to be a cosmological constant. As a result, the Friedmann equations are modified to :

$$H^2 = (\frac{\dot{a}}{a})^2 = \frac{8\pi G}{3}\rho + \frac{\Lambda}{3} - \frac{k}{a^2} \tag{1.13}$$

Λ was used to balance the curvature in order to have a static universe. Its unit is $[time]^{-2}$. The term Λ also affects the acceleration equation as follow:

$$\frac{\ddot{a}}{a} = -\frac{4\pi G}{3}(\rho + 3p) + \frac{\Lambda}{3} \tag{1.14}$$

To find a static ($\dot{a} = 0$) solution in Einstein static universe, the parameters ρ, p, and Λ are set to be nonnegative. When Λ is positive, $\ddot{a}$ will be positive which implies a repulsive force.

Cosmological model with Λ

$$\Omega_\Lambda = \frac{\Lambda}{3H^2} \tag{1.15}$$

Λ is constant but Ω_Λ is time-dependent due to its dependence on H. Rearranging the Friedmann equation, we than have

$$\Omega + \Omega_\Lambda - 1 = \frac{k}{a^2 H^2} \tag{1.16}$$

In a flat universe (k=0) gives

$$\Omega + \Omega_\Lambda = 1 \tag{1.17}$$

Different values of k and Ω imply different curvatures and fates of the universe.

Open universe ($k = -1$): $0 < \Omega + \Omega_\Lambda < 1$ The universe is underdense in this case.

Closed universe ($k = 1$): $\Omega + \Omega_\Lambda > 1$ This scenario made the overdense universe.

In the ΛCDM model, the Ω value is dominated by the cold dark matter and dark energy. This model has zero spatial curvature, $\Omega_m = 0$ with $\Omega_m = 0.26 \pm 0.03$, $\Omega_\Lambda = 0.74 \pm 0.03$.

1.1.4 The cosmic microwave background and the growth of large scale structure

The Big Bang model is used to explain the very beginning state of the Universe. According to the model, the Universe expands from a very hot and dense state in the past about 15 billion years ago. After 300,000 years of the Big Bang, the temperature of the universe cooled to T $\approx$ 4000 K. The matter does not have enough energy to remain ionized in this state. When photons and electrons bind together, it reduces the cross-section of

Compton scattering. The radiation then expands and cools to a black body temperature (2.7 Kelvin). At this temperature, it shows a peak signal at microwave frequencies ($\approx$ 1- 1000 GHz) called the Cosmic Microwave Background (CMB). This radiation was first detected in 1965 by the observations of Arno Penzias and Robert Wilson. In observations over the sky, it is seen to be the same from all directions. This causes problems. If the universe is so smooth, what caused the growth on the large-scale structure? It was suggested to be the effect of density fluctuations in the early universe.

In the observations, any objects further than the particle horizon, the most distant object that could have affected the observer, are unable to contact with the observer. From the scattering surface, no physical processes will happen on scales larger than 2 degrees as seen from Earth (Jones, 1998). It is thought that the matter perturbations are affected by the fluctuations on scales greater than $\theta \approx 2$ degrees in the recombination era. Within 10^{-34} seconds after Big Bang, these fluctuations probably originate in the quantum fluctuation of a scalar field. The CMB observations allow us to understand the initial density perturbations from the large-scale universe. We can use it to investigate the components of the structure as well as the nature of the universe (Harrison, 1970; Peebles & Yu, 1970; Zel'Dovich, 1970).

The distribution of the mass in the universe can be quantified by the density perturbations as a function of mass densities (ρ):

$$\delta(x) \quad = \quad \frac{\rho(x) - < \rho >}{< \rho >} \tag{1.18}$$

At early times, the perturbation scale depends on the expansion factor $a(t)$.

$$\delta(x) \quad \propto \quad a(t) \tag{1.19}$$

where $a(t)$ is the expansion factor. The amplitude of the perturbation is affected by gravity. For instance, the formation of stars, galaxies and clusters are caused by the collapse of perturbation structure. The autocorrelation function of the density field which

can be used to measure the clustering properties of the visible component of the density field is defined as :

$$\xi(r) = \langle \delta(x)\delta(x+r) \rangle \tag{1.20}$$

r is a separation between two local densities. The clustering of the luminous components with the correlation function can link to the evolution of the galaxy. The dominant peak of the luminous component may extend our understanding of how the dark matter is distributed. The bias parameter, b, gives information on how dark matter is related to the galaxy clusters (Kaiser, 1987).

1.2 Galaxy clustering and redshift-space distortions

Observing objects at high redshift provides a precise three-dimensional view of the universe (Kaiser, 1987). In cosmology, the third dimension is redshift not radial distance. The measured redshift is not only affected by the expansion of the universe, but also includes the effect of the peculiar velocities (da Angela, 2005). Redshift-space refers to a map where radial distance estimates are based on redshifts which include the effect of peculiar velocity. Real-space refers to the true positions of the measured object. In an inhomogeneous Friedmann universe, peculiar velocities distort clustering of galaxies in redshift space (Kaiser, 1987). These distortions are caused by the galaxy motions on large-scales because the true mass distribution is affected by gravity (Guzzo, 1997).

Due to the effect of the random motions within the objects, the two-point correlation function in redshift space differs from the correlation in real space. On small scales, particles at the same distance tend to have a slightly different measured redshift. The structures along the line-of-sight tend to be extended with respect to the observer, which is called finger-of-God effect. At large scales, the peculiar motion due to gravitational infall will make the objects on the far side of an overdensity appear closer and those on

the near side appear further away, making the cluster appear flattened in the redshift direction. These effects are called redshift-space distortion.

According to Kaiser et al. (1987), by calculating the infall parameter, β, from the large-scale clustering in real and redshift space, the clustering of dark matter can be revealed. The power spectrum distorted by the peculiar velocity field is defined as (Eq. 1.13 -1.17 in da Angela et al. 2005) :

$$P_{gal}(k_s) \quad = \quad P_{gal}(k_r)(1+\beta\mu^2)^2 \tag{1.21}$$

Here we denote the real space coordinate as r and the redshift space coordinate as s. β measures the increase in clustering from large-scales caused by redshift space distortions. The cosine between the line-of-sight vector and velocity vector is defined as μ. The linear redshift-space distortion derived by Kaiser et al. (1987) can be written as:

$$\xi_{gal}(s) \quad = \quad \xi_{gal}(r)(1+\frac{2}{3}\beta+\frac{1}{5}\beta^2) \tag{1.22}$$

Then β is defined by

$$\beta \quad = \quad \frac{f(\Omega_m(z),\Omega_\lambda(z),z)}{b} \tag{1.23}$$

The term bias, b, is related to the luminous matter clustering to the dark matter ($b^2 = \xi_{gal}/\xi_{mass}$) (da Angela, 2005).

In the case of flat universe, the growth structure can be defined as :

$$f \quad \approx \quad \Omega_m(z)^{0.6} + \frac{1}{70}(1-\frac{1}{2}\Omega_m(z)(1+\Omega_m(z))) \tag{1.24}$$

or approximately

$$f \approx \Omega_m(z)^{0.6} \tag{1.25}$$

In order to understand more of the effect of z-space distortions, we need to account for the β parameter. The infall velocities can be derived by starting from Newtonian Gravitation. Following Kaiser et al. 1987, the acceleration vector is given by

$$\mathbf{a_r} \equiv \int_{V_r} d^3r \Delta(\mathbf{r}) \frac{\mathbf{r}}{r^3} \tag{1.26}$$

where V_r is the survey volume and $\Delta(\mathbf{r})$ $(= \frac{\delta\rho_m}{\rho_m})$ is the density contrast. Then from linear theory, the peculiar velocity of the particle at the origin is

$$\mathbf{v} = -\frac{2}{3}\frac{G\rho_{crit}\mathbf{a}}{H_0} f(\Omega) \tag{1.27}$$

Assuming a sphere of radius r for V_r, and $\frac{\delta\rho_m}{\rho_m}$ is constant in V_r. Solving the two equations above to find $\mathbf{v}$, the expression for the infall velocity of the biased particles is

$$\mathbf{v} = -\frac{1}{3}\mathrm{H_0}\mathbf{r}\ \Omega^{0.6}\frac{1}{b}\frac{\delta\rho_g}{\bar{\rho}_g}\hat{r} \tag{1.28}$$

Here we have also used $\rho_{crit} = \frac{3H_0^2}{8\pi G}$ and $\frac{\delta\rho_m}{\rho_m} = \frac{1}{b}\frac{\delta\rho_g}{\bar{\rho}_g}$. Since $\mathbf{v_{Hubble}} = H_0\mathbf{r}$, this gives

$$\frac{\mathbf{v_{infall}}}{\mathbf{v_{Hubble}}} = -\frac{1}{3}\frac{\delta\rho_g}{\bar{\rho}_g}\beta\hat{\mathbf{r}} \tag{1.29}$$

for the infall velocity of a galaxy at a distance r from a centre of a spherical overdensity.

As pointed out by da Angela et al. (2005), there are several ways to evaluate β. For instance, we can use the ratio of the correlation function in redshift and real space or we can use the ratio of the quadrupole to monopole moments of the redshift-space correlation

function. But in this thesis, we choose the simpler method, substituting $\xi(s)$ and $\xi(r)$ values into the equation, $\xi_{gal}(s)/\xi_{gal}(r) = (1 + \frac{2}{3}\beta + \frac{1}{5}\beta^2)$. From this equation, the infall parameter can be derived.

Chapter 2

Galaxy Evolution and Feedback via Lyman Break Galaxies

To understand the evolution of the Universe, we need to look back to the initial state of the Universe which can be linked to what we see today. For instance, we can observe galaxies at high-redshift to understand their formation and evolution. This will let us understand more about early star formation activity in the Universe as well as the physical processes of cosmic reionization in the IGM.

2.1 The Universe at high redshift

In order to examine the evolution of stars and galaxies, we need to observe the young Universe. It is interesting to study the galaxies at high-redshift. The higher redshift, the younger the Universe. We will improve our understanding of the formation and evolution of galaxies if we can actually observe them at high redshift. The problem is, how can we detect them?. Before the mid 90s, it was difficult to identify the high-redshift galaxies. Very distant galaxies are faint since they emitted their light at a large distance. Moreover, it was also hard to recognise their absorption and emission spectral features.

Thanks to the developments in instrumentation, it is now easier to explore star forming galaxies in the high-redshift Universe. In recent years, we can observe sources at very high-redshift. As shown in Figure 2.1, the spectrum of a very high-redshift QSO at z = 6.43, a

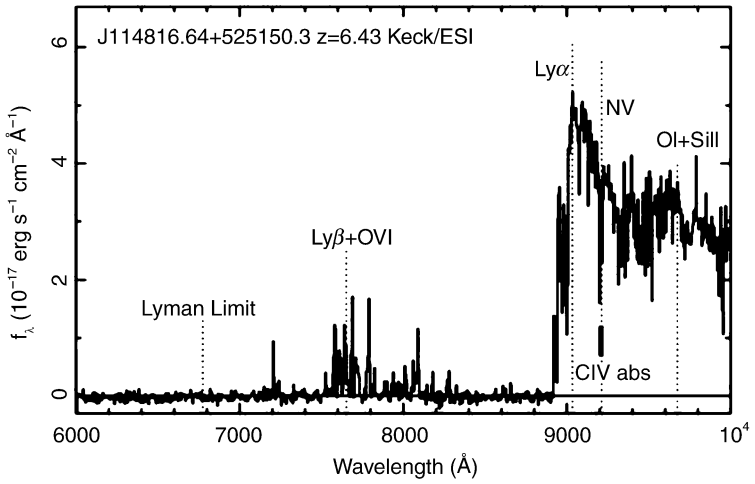

Figure 2.1: (from Schneider, 2006): Spectrum of a QSO at z = 6.43 which was detected by the Sloan Digital Sky Survey. We can see the redshifted Lyα line clearly. Most radiation bluewards of the Lyα line is absorbed but Lyβ emission line still getting through. The spectral flux is almost zero at the wavelength below 7200 $\mathring{A}$. This shows a very strong absorption due to Lyman limit at 912 $\mathring{A}$.

time when the Universe was only $\approx$ 1 Gyrs old, can be observed (Schneider, 2006). There are several strategies to detect high-redshift galaxies (Nilsson, 2007). One of the most useful tools is Lyman Break Galaxy selection.

2.2 The Lyman-Break Method

The Lyman Break technique allows us to understand more about the properties of the high-redshift galaxy populations (Pettini, 2007), which can be linked to what we have seen today. Galaxies at interesting redshifts can be chosen by a photo-metric selection method. It was first measured and used successfully in the mid-1990s by Steidel et al. (1992) to collect and identify high-redshift quasars (Pettini, 2007). They used this method

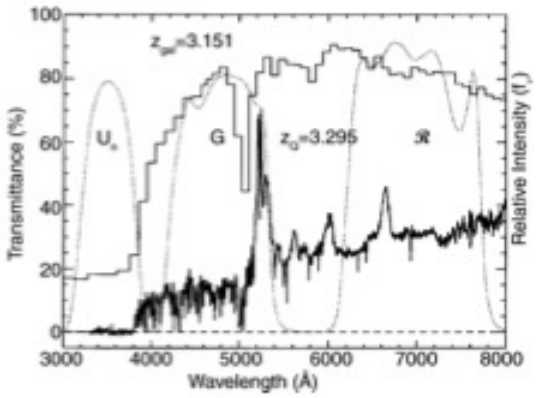

Figure 2.2: (from Schneider, 2006): The histogram shows the synthetic spectrum of a galaxy at z = 3.15. The spectrum shows a break at $\lambda \leq 912(1+z)\mathring{A}$. The transmission curves of three broad-band filters are illustrated by dotted lines. From U_n GR filter, Lyman Break will have redder colour in show U_n-R filter and blue colour in G-R.

to observe galaxies at z $\approx$ 3 and search for Lyman absorption systems from QSOs line-of-sight. Galaxies at z $\approx$ 3 were identified using deep optical imaging in the U, G and R bands.

From the fact that the most abundant ion in the Universe is neutral hydrogen at ground state, light at wavelengths shorter than 912 $\mathring{A}$ is heavily absorbed by hydrogen and it is very difficult to escape from a galaxy. This absorption makes a break, called a Lyman Break, in the spectrum of galaxies. We can determine the redshift of the light from a source by this Lyman break. The cut-off energy represents the ionization from the single electron of a hydrogen atom. This also happens in intergalactic absorption. QSO spectrum has a Lyα forest and Lyman-limit absorption features. At $\lambda < 1216\mathring{A}$, the high-redshift source will emit photons in its continuum and these photons will be neutral absorbed by intergalactic gas. This also happens to all source photons at $\lambda < 912\mathring{A}$ in the rest-frame wavelength. In conclusion, a break feature in high-redshift galaxy spectra can be detected at 1216 $\mathring{A}$. Moreover, the intergalactic absorption and the interstellar

Blue Filter	Red Filters	Redshift range
U	B, G, R, V	2.5-3.5
B	G, R, V	3.5-4.5
V	i, z	4.5-6.0
i	z, J	6.0-7.5
Z	J, H, Ks	7.5-11.5
J	H, Ks	11.5-15.5

Table 2.1: (from Nilsson, 2007): The filters that can be used in Lyman Break technique at different redshift.

medium absorption from galaxies themselves suppress the fraction of ionizing photons at $\lambda < 912\mathring{A}$. This is a reason why such a small fraction of this ionizing radiation is detected (Schneider, 2006).

Using these facts, a detection of galaxies at redshift higher than $z = 3$ can be made. Three broad-band filters are usually applied to non-overlaping wavelengths, $\lambda_1 \pm \Delta\lambda_1 \leq \lambda_2 \pm \Delta\lambda_2 \leq \lambda_3 \pm \Delta\lambda_3$. If central wavelengths $\lambda_1 \leq (1+z)912\mathring{A} \leq \lambda_2$, we should see a galaxy containing young stars moves bluewards to the filters λ_2 and λ_3 (see Figure 2.2) and disappears in λ_1 filter because of the absorption (Schneider, 2006). As mentioned above, galaxies selected like this one are termed Lyman Break Galaxies (LBGs). The Lyman Break method has been applied to several redshifts as shown in Table 2.1. Different selections can be made with the different filters.

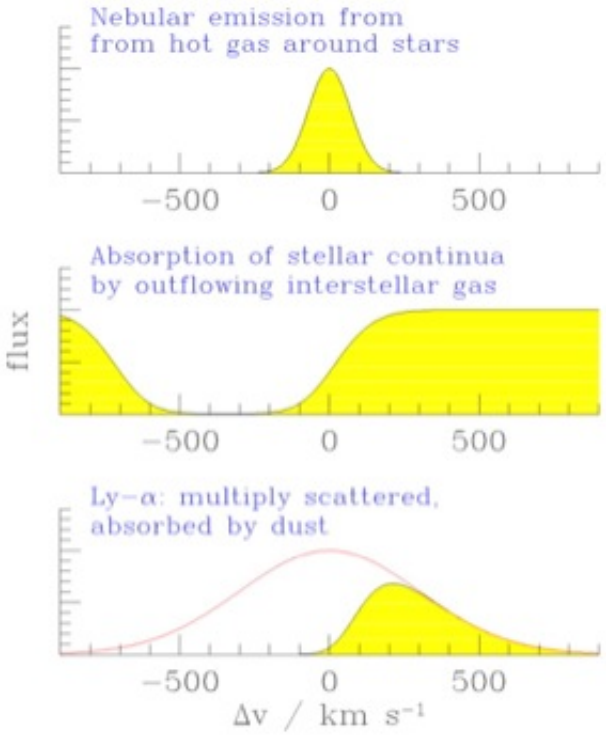

Figure 2.3: (from Adelberger, 2003): shows three types of lines to indicate the redshifts. First, nebular emission lines from hot gas around stars which are detected through the near-IR spectroscopy of 27 LBGs tend to have higher redshifts than interstellar medium. Second, interstellar medium absorption lines, which are generated by outflowing, tend to have lowest redshifts. Third, Lyα has highest redshifts. At the backside of the outflowing material, Lyα photons that scattered off were detected. Adelberger et al. (2003) suggest that the true redshifts are indicated by nebular lines since the gas which is depend on nebular emission and hot stars should be in the same region. The systemic redshift of the galaxy from its rest-frame spectrum was estimated by using the correlations between nebular line redshifts and UV spectral characteristics from 27 LBGs.

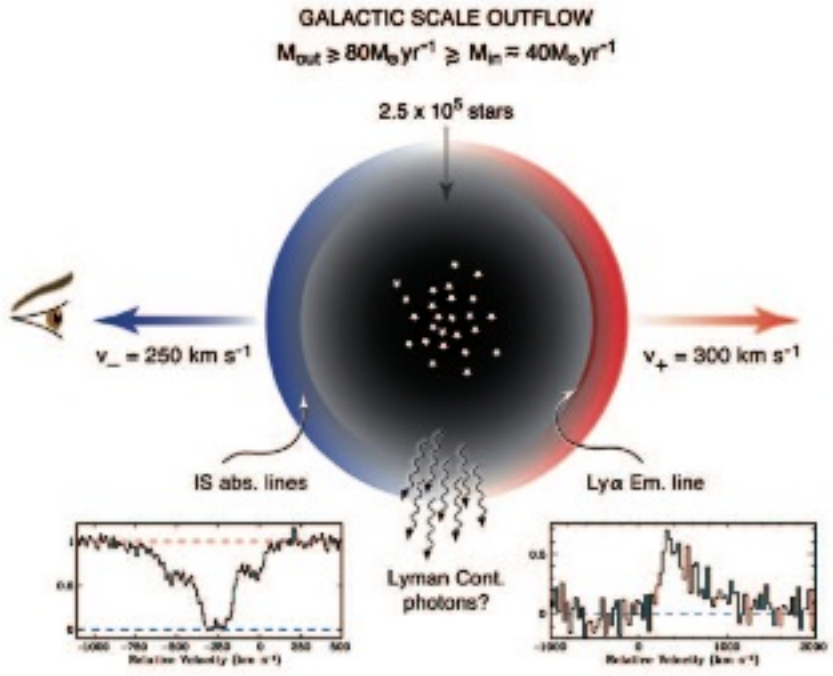

Figure 2.4: (from Pettini, 2007): shows the outflows in star-forming galaxies. Interstellar absorption lines tend to have blue-shift relative to the systemic velocity of the stars since they may be blown out by the wind. Whereas in emission regions, the Lyα emission line tend to have the higher redshifts.

2.3 Feedback of Star-Forming Galaxies: winds and outflows

Observations show that different galaxy absorption and emission lines give different redshifts (Pettini, 2007). Lyman-break galaxy (LBG) redshifts can be measured by considering interstellar absorption, nebular emission, and Lyα emission (see Figure 2.3). The nebular emission lines from hot gas around stars tend to have the higher redshifts. Interstellar medium absorption lines, which are generated by outflowing gas, tend to have

lowest redshifts or blue-shifted relative to the systemic velocity (see Figure 2.4). The Lyα emission line and the interstellar absorption line are several hundred kms^{-1} different in velocity. This is suggested to be evidence for feedback or modulation of the efficiency of star formation (Pettini, 2007). Feedback is a key factor of current models of galaxy formation. Many models need feedback to regulate the star formation activity and also limit the number of low-mass galaxies production. The cosmological smoothed particle hydrodynamics (SPH) simulations from Springel & Hernquist (2003) show that galactic outflow from supernova feedback is the important part to recreate the star formation. Models without some sort of feedback may produce too small disk galaxies and create too strong X-Ray background (Theuns 2002 and Bielby 2008).

These large-scale outflows lead us to think about their effects on galaxies and their surroundings. Some suggest that outflows can be used to explain the metallicity relation and the relationship between gas fraction and metallicity. More observations may help us to understand more about how supernova kinetic energy affects the ambient ISM or what is the relation rate of gas inflow and outflow (Pettini, 2007). Many studies are also trying to study the effect of galaxy-wide winds on the metal in IGM by looking at the properties of galaxies seen from line-of-sight of background QSOs.

2.4 Lyα-LBG cross correlation

A survey at redshift z $\sim$ 3 is interesting for many reasons. Firstly, it is not difficult to identify the galaxies at z $\sim$ 3 using deep imaging. Moreover, a strong absorption line generated by intergalactic gas can be observed from the ground in optical high-resolution spectra of background QSOs. It has been suggested from Adelberger et al. (2003) that we may see the supernova-driven wind at high redshift, where galaxies have a higher star formation rates and were less massive than at low redshift.

Adelberger et al. (2003 and 2005) conducted significant observations to study the

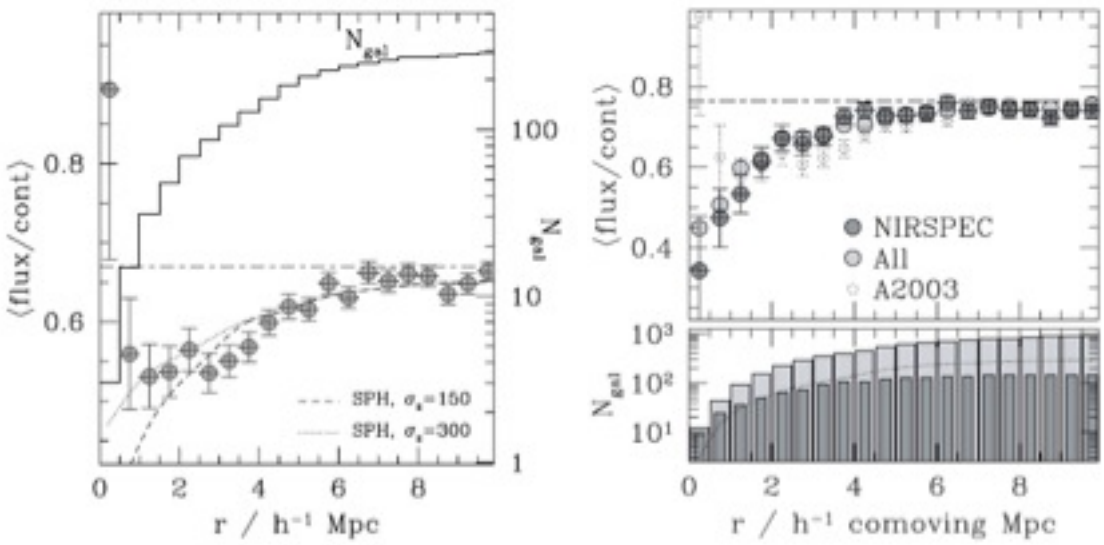

Figure 2.5: (a : left) Adelberger et al. (2003) illustrates the mean Lyα transmissivity as a function of comoving distance in Mpc from LBG. The mean flux increases and reaches the mean transmissivity of 0.67 at $r > 6h^{-1}$ comoving Mpc. However, in the spectral samples that lie within 0.5 h^{-1} comoving Mpc from LBG, the flux decreases. This implies that at a distance close to LBGs, IGM contain less neutral hydrogen. This lead to the possible reason that feedback winds may heat up and evacuate the Lyα clouds. (b : right) shows A05 cross-correlation of Lyα-LBG along the line of sight to 23 QSOs. The flux increases and reaches the mean transmissivity of 0.765 at $r > 6h^{-1}$ comoving Mpc. It continues to decline with respect to more nearly galaxies at $r < 2h^{-1}$ Mpc.

effect of galactic winds on the IGM (see Figure 2.5). They used high resolution spectra of six background QSOs at $z \sim 3$ to study the correlation function of LBGs and their correlation with Lyα and CIV absorption systems. They found a decrease in flux at the distance near LBGs ($r < 0.5h^{-1}$ comoving Mpc). These implied a lack of neutral hydrogen near these galaxies.They claimed this result to be evidence of superwinds from star-forming galaxies. Two years later, they found a different result using the similar observations with a better statistical significance. The later result showed strong Lyα absorption close to LBGs.

Based on Adelberger's observations, the proximity effect, the lack of Lyα absorption near the background QSO (Rauch, 1998), is still an issue, since it is still unclear whether galactic winds have effects on the galaxy and its surroundings or not. This motivation from the results of Adelberger et al. (2003, 2005) leads us to try to extend their work on the correlation between QSOs and LBGs at high redshift.

2.5 Thesis outline

In this thesis, we aim to study the clustering properties of galaxies at z $\approx$ 3 and the relationship between galaxies and the IGM at these redshift by measuring their correlation function. The structure of the rest of this thesis is as follows. We have already described backgrounds of modern cosmology in Chapter 1 and the backgrounds of galaxy evolution and feedback in this Chapter. In Chapter 3, we use the combination data from the VLT LBG Survey (Bielby, 2008) and Steidel et al. (2003) to perform LBG-LBG correlation function. We aim to (a) roughly estimate β from $\frac{\xi(s)}{\xi(r)}$, (b) estimate LBG bias factor in standard cosmology at z = 3. In Chapter 4, we use Lyα-LBG correlation function and LBG-CIV correlation function to study the interaction between galaxies and the IGM at z $\sim$ 3. We attempt to (a) investigate the effect of feedback on the LBG-Lyα cross correlation, (b) also look at metal lines in the QSO spectra. We want to compare the LBG-CIV cross-correlation with LBG-LBG $\xi(s)$ to see if they are distributed like LBG.

In Chapter 5, we employ simulations to create Lyα spectra and Galaxies in order to calculate Lyα-LBG cross-correlation using the same method in Chapter 4. Our main aims in Chapter 5 are therefore to study (a) LBG-LBG $\xi(s)$ to see if we can detect the effects of peculiar velocities and possibly feedback by comparing real and redshift space correlation function, (b) LBG-Lyα $\xi(s)$ to understand more about outflow and feedback. Chapter 6 provides the conclusions from this work.

Chapter 3 | *LBG-LBG correlation function*

3.1 Introduction

The clustering properties of galaxies at z $\approx$ 3 and the relationship between galaxies and the IGM at this redshift are studied by considering their correlation function. We aim to (a) roughly estimate β from $\xi(s)/\xi(r)$ and hence estimate the LBG bias factor, b, in the standard cosmology at z = 3.

3.2 The LBG data

The LBGs used in the calculation are obtained from the observation of Bielby et al. (2008). They observed LBGs that are located around five fields of bright QSOs which are Q0042-2627 (z = 3.29), SDSS J0124+0044 (z = 3.84), HE0940-1050 (z = 3.05), SDSS J1201+0116 (z = 3.23) and PKS2126-158 (z = 3.28). The details are summarized in Table 3.1, Table 3.2 and Table 3.3. The complete data can be found in Bielby et al. (2008). In total we have 1109 LBGs at $2 < z < 3.5$. We also included LBGs from the Steidel et al. (2003) Keck samples. There are 813 LBGs at redshift $2.67 \leq z \leq 3.25$ in this sample (see Table 3.4).

Name	R.A.	Dec	Facility
Q0042-2627	11.1414583	-26.1888611	CTIO/MOSAIC2, VLT/VIMOS
SDSS J0124+0044	21.0157089	0.7424445	CTIO/MOSAIC2
HE0940-1050	145.722500	-11.0736113	CTIO/MOSAIC2
SDSS J1201+0116	180.434880	1.2698889	KPNO/MOSAIC, VLT/VIMOS
PKS2126-158	322.300625	-15.644674	CTIO/MOSAIC2

Table 3.1: (from Bielby 2008): The centres of five spectroscopic fields and the imaging data sources.

3.3 Redshift Space Correlation Function

The probability of finding the clustering of a galaxy population at redshift-space separations is measured by the redshift-space correlation function, $\xi(s)$.

$$\xi(s) \quad = \quad \frac{Nr}{Ng}\frac{< DD(s) >}{< DR(s) >} - 1 \tag{3.1}$$

where $< DD(s) >$ is the average number of LBG-LBG pairs. $< DR(s) >$ is the number of pairs of LBG-random LBG at the separation, s. The factor Nr/Ng is the ratio of the number of random and data points.

As mentioned above, we used observed LBG data from Bielby et al. (2008) and Steidel et al. (2003). The total number of LBGs from both surveys is 1922 in 1.56 deg^2. Random LBGs are also obtained from Bielby et al. (2008). They generated random LBGs for each field, consistent with the overall observed LBGs. A weight function is applied to DD pairs at the θ separation within $2^{'}$ to account for slit-slit overlaps in the VIMOS LBG

Name	Sub-field	R.A.	Dec
Q0042-2627	f1	11.2964163	-26.0727787
Q0042-2627	f2	10.9887505	-26.0727787
Q0042-2627	f3	11.2931252	-26.3185825
Q0042-2627	f4	10.9832087	-26.3211384
SDSS J0124+0044	f1	21.1742496	0.8718889
SDSS J0124+0044	f2	20.8835831	0.8703055
SDSS J0124+0044	f3	20.8803749	0.6172222
SDSS J0124+0044	f4	21.1744175	0.6142778
HE0940-1050	f1	145.53342	-11.1372776
HE0940-1050	f2	145.83971	-11.1430559
HE0940-1050	f3	145.83992	-10.9088335
SDSS J1201+0116	f1	180.55838	1.1527500
SDSS J1201+0116	f2	180.29170	1.1527500
SDSS J1201+0116	f3	180.29184	1.4027222
SDSS J1201+0116	f4	180.55862	1.4022223
PKS2126-158	f1	322.49820	-15.5250559
PKS2126-158	f2	322.19250	-15.5249720
PKS2126-158	f3	322.50171	-15.7884169
PKS2126-158	f4	322.19278	-15.7866392

Table 3.2: (from Bielby 2008): The details of spectroscopic data of sub-fields.

Field	Subfields	z >2 galaxies	z> 2.0 QSOs	z<2 galaxies	stars
Q0042-2627	4	343 (0.38deg^{-2})	1	83	3
SDSS J0124+0044	4	255 (0.28deg^{-2})	0	51	16
HE0940-1050	3	180 (0.27deg^{-2})	0	26	33
J1201+0116	4	133 (0.15deg^{-2})	5	122	63,
PKS2126-158	4	238 (0.27deg^{-2})	3	24	115
Total	19	1149(0.27deg^{-2})	9	306	227

Table 3.3: (from Bielby 2008): The summarized observational data of VLT VIMOS LBGs.

observation. After doing this, we obtained the original correlation function at $\theta \approx 0.1^{'}$. The weighted function is defined in Bielby et al. (2008) as:

$$W(\theta) = \frac{1}{1 - 0.0738\theta^{-1.052}} \tag{3.2}$$

This was obtained by comparing the 2-D correlation function of the input galaxy catalog with the correlation function of the galaxies targeted with slits.

3.4 Results

The LBG-LBG $\xi(s)$ from the VLT survey, the Keck survey, and the Bielby et al. (2008) VLT calculation are shown in Figure 3.1 (a). The error bars are calculated by Poisson error estimates, as $\Delta\xi(s) = \frac{1+\xi(s)}{\sqrt{DD}}$. Comparing the results from the VLT LBG data, our calculation (filled circles) shows the same clustering as Bielby et al. 2008 (open diamonds) especially at the separation $s > 8h^{-1}Mpc$ but it shows slightly lower clustering

Field	Dimensions (arcmin^2)	Number of LBGs
Q0000-263	3.69 ×5.13	15
CDFa	8.80×8.91	34
CDFb	9.05×9.10	20
Q0201+1120	8.69 ×8.72	21
Q0256-000	8.54×8.46	42
Q0302-003	6.50 ×6.90	40
B20902+34	6.36×6.57	30
Q0933+2854	8.93×9.28	58
HDF-N	8.62×8.73	53
Westphal	15.0×15.1	176
Q1422+2309	7.28×15.5	109
3C 324	6.65×6.63	11
SSA22a	8.74×8.89	50
SSA22b	8.64 ×8.98	35
DSF2237a	9.08×9.08	39
DSF2237b	8.99 ×9.08	42
Q2233+1341	9.25×9.25	38
Total	0.38deg^{-2}	813

Table 3.4: LBG survey of Steidel et al. (2003).

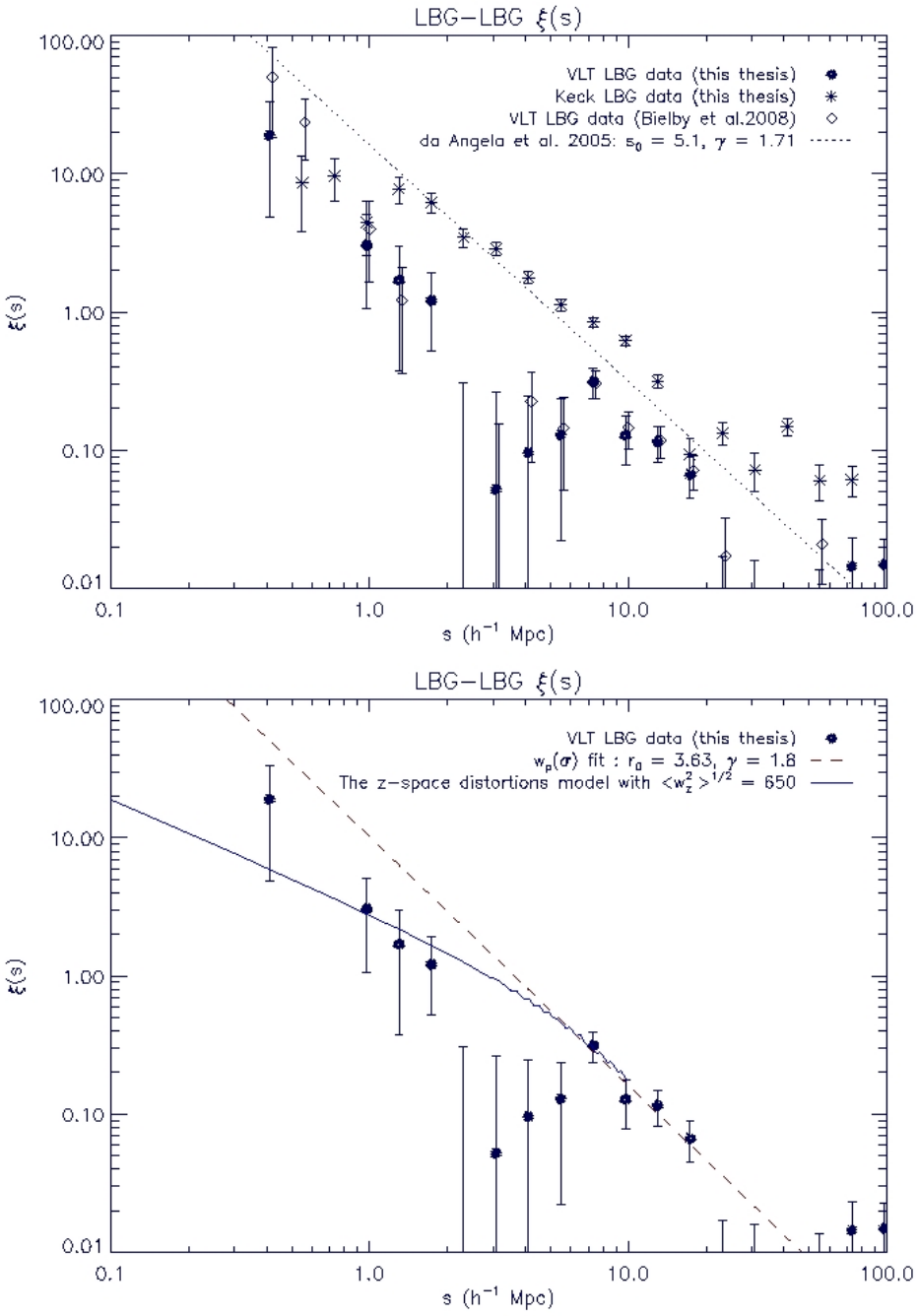

Figure 3.1: a) top : The LBG-LBG $\xi(s)$ from VLT data (this thesis : filled circles, Bielby et al. (2008) : open diamonds) and Keck data (asterisks). The dotted line is the fit to the Keck $\xi(s)$ from da Angela et al. 2005 with $\gamma = 1.71$ and $s_0 = 5.1h^{-1}$ Mpc. b) bottom : The VLT LBG-LBG $\xi(s)$ from our results. The dashed line is $\xi(r)$, fitted from combined $w_p(\sigma)$ of Bielby et al. 2008 with $\gamma = 1.8$ and $r_0 = 3.63h^{-1}$ Mpc. The $z-$space distortions model from da Angela et al. (2005), here assuming $\gamma = 1.8$, $r_0 = 3.63h^{-1}$ Mpc, $\beta = 0.2$, and $< w_z^2 >^{\frac{1}{2}} = 650 kms^{-1}$, is shown by blue solid line.

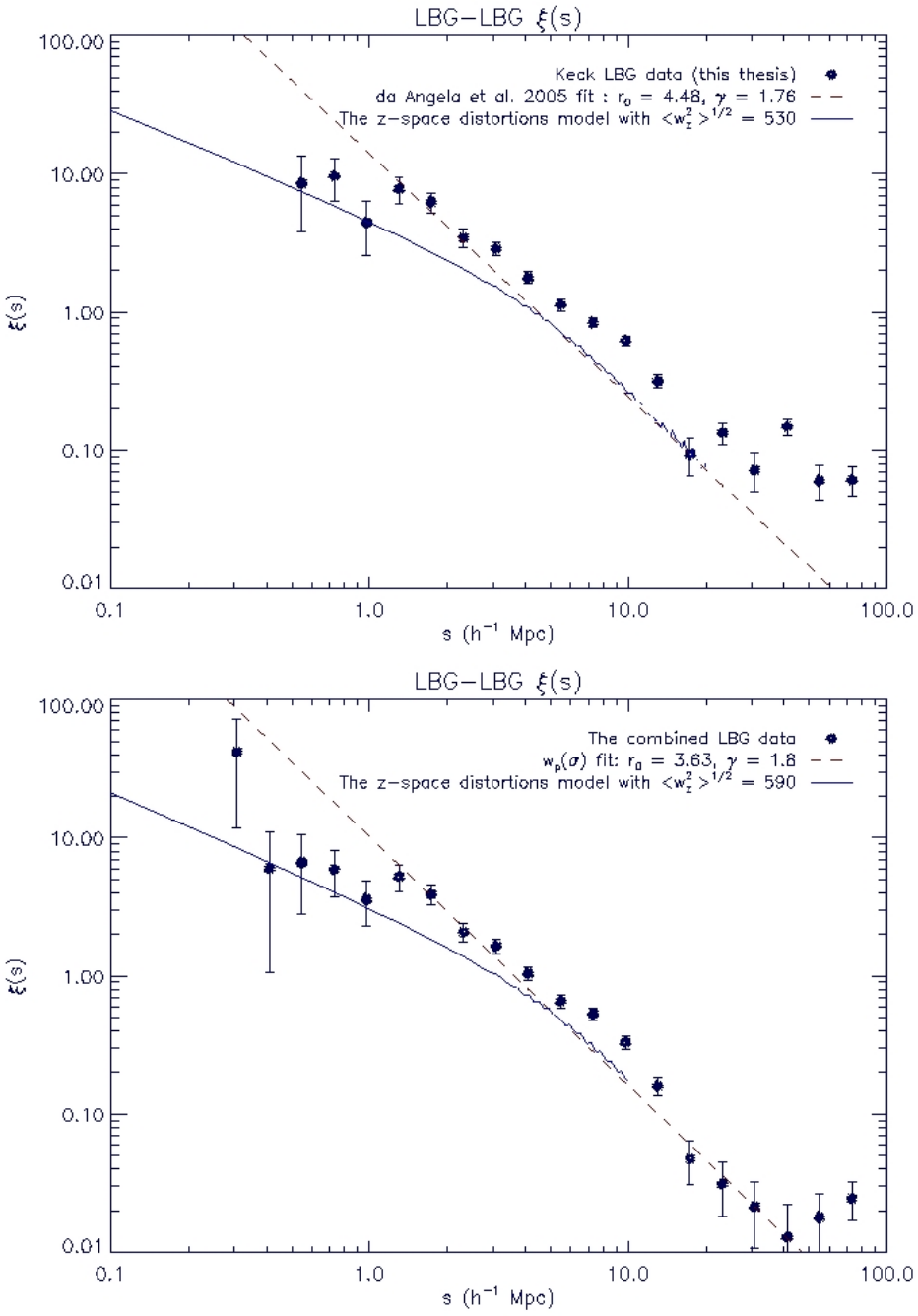

Figure 3.2: a) top : The LBG-LBG $\xi(s)$ from the Keck data (filled circles). The dashed line is $\xi(r)$ from $w_p(\sigma)$ of da Angela et al. 2005 with $\gamma = 1.76$ and $r_0 = 4.48h^{-1}$ Mpc. The blue solid line shows the $z-$space distortions model from da Angela et al. (2005), here assuming $\gamma = 1.76$, $r_0 = 4.48h^{-1}$ Mpc, $\beta = 0.25$, and $< w_z^2 >^{\frac{1}{2}} = 530kms^{-1}$. b) bottom : The combined LBG-LBG $\xi(s)$ (filled circles). The dashed line is $\xi(r)$, fitted from combined $w_p(\sigma)$ of Bielby et al. 2008 with $\gamma = 1.8$ and $r_0 = 3.63h^{-1}$ Mpc. The blue solid line is plotted by assuming $\gamma = 1.8$, $r_0 = 3.63h^{-1}$ Mpc, $\beta = 0.2$, and $< w_z^2 >^{\frac{1}{2}} = 590kms^{-1}$.

LBG data	$r_0(h^{-1}$ Mpc)	γ	β	$< w_z^2 >^{\frac{1}{2}}$ (kms^{-1})
VLT	3.63	1.8	0.2	650
Keck	4.48	1.76	0.25	530
VLT + Keck	3.63	1.8	0.2	590

Table 3.5: Fitting parameters for $z-$space distortions model from da Angela (2005).

below $8h^{-1}Mpc$. This may be caused by the correction of some LBG redshift estimates. In our calculation, we use some updated LBGs redshift estimates. We then compared the result from Keck data (asterisks) with the fit from da Angela et al. 2005 (dotted line) who used 813 LBGs from Steidel et al. (2003) to calculate $\xi(s)$. The dotted line is plotted assuming $\gamma = 1.71$ and $s_0 = 5.1h^{-1}$ Mpc. At separations below $3h^{-1}$ Mpc, our results show lower clustering than in da Angela et al. (2005) but we see higher clustering at the distance $> 3h^{-1}$ Mpc. This difference is possibly caused by the estimator that we used to calculate $\xi(s)$. We use the simple form of estimator as shown in Eq. (3.1), while da Angela et al. (2005) used the Landy-Szalay estimator to calculate $\xi(s)$. We also compared our VLT result with the Keck result. We see lower clustering from the VLT sample at scales $< 10h^{-1}$ Mpc. It is possible that our higher redshift errors may cause this difference. The error bars from the VLT results are higher than in Keck. We then tested the effect of redshift errors by using the $z-$space distortions model from da Angela et al. (2005) with the parameters shown in Table. 3.5. We used a combination of the error on the spectral feature measurement to estimate the peculiar velocity. We combined the uncertainties on the estimation of the intrinsic peculiar velocity ($\approx 400kms^{-1}$), the measurement error ($\approx 150 - 300kms^{-1}$), and the error caused by outflows ($\approx 200kms^{-1}$) respectively. We then have $< w_z^2 >^{\frac{1}{2}} = \sqrt{400^2 + 2(150)^2 + 2(200)^2} = 530kms^{-1}$ and $< w_z^2 >^{\frac{1}{2}} = \sqrt{400^2 + 2(300)^2 + 2(200)^2} = 650kms^{-1}$ for the Keck and the VLT data respectively. The peculiar velocity for the combined data is averaged from the Keck and the VLT data which is $< w_z^2 >^{\frac{1}{2}} = \sqrt{530^2 + 650^2} = 590kms^{-1}$.

Figure 3.1 (b) shows our VLT results (filled circles) compared with fitting models. The dashed line is $\xi(r)$, fitted from combined $w_p(\sigma)$ of Bielby et al. 2008 with $\gamma = 1.8$ and $r_0 = 3.63h^{-1}$ Mpc. We plotted the blue solid line by using the $z-$space distortions model from da Angela (2005). The model works by adding the effects of coherent large-scale infall (β) to the real-space correlation function $\xi(r)$ and then more importantly adding the distribution of the small-scale pairwise peculiar velocities ($< w_z^2 >^{\frac{1}{2}}$). From da Angela (2005), the $\xi(\sigma, \pi)$ model is first calculated by using input power-law $\xi(r)$, infall parameter β and peculiar velocities $< w_z^2 >^{\frac{1}{2}}$. Then $\xi(s)$ is obtained by computing the average $\xi(\sigma, \pi)$ in constant annuli of radius s. We employed model I of da Angela et al. (2005) by assuming $\gamma = 1.8$, $r_0 = 3.63h^{-1}$ Mpc, $\beta = 0.2$, and $< w_z^2 >^{\frac{1}{2}} = 650kms^{-1}$. This velocity dispersion including measurement error comes from Bielby et al. (2008). Similar to Figure 3.2 (a) and (b), we applied the $z-$space distortions model to the Keck and the combined data respectively. The blue solid line in Figure 3.2 (a) is plotted by using the $\xi(r)$ fit of da Angela et al. 2005 with $\gamma = 1.76$, $r_0 = 4.48h^{-1}$ Mpc, $\beta = 0.25$, and $< w_z^2 >^{\frac{1}{2}} = 530kms^{-1}$. Figure 3.2 (b) shows LBG-LBG $\xi(s)$ from the combined data. We see higher clustering with smaller error bars in the combined data. The blue solid line is plotted by using $\gamma = 1.8$, $r_0 = 3.63h^{-1}$ Mpc, $\beta = 0.2$, and $< w_z^2 >^{\frac{1}{2}} = 590kms^{-1}$. This average velocity dispersion comes from the peculiar velocity estimation of Keck and VLT which have the value of $< w_z^2 >^{\frac{1}{2}} = 530, 650kms^{-1}$ respectively. We see less effects of the peculiar velocity in the combined data compared to the VLT data because the better redshift estimation in Steidel et al. (2003).

3.5 Estimating β

We next use the LBG-LBG correlation function in redshift and real space to measure the infall parameter, β, at $z = 3$. The ratio of $\xi(s)/\xi(r)$ gives a rough β by using the simpler form of (da Angela, 2005):

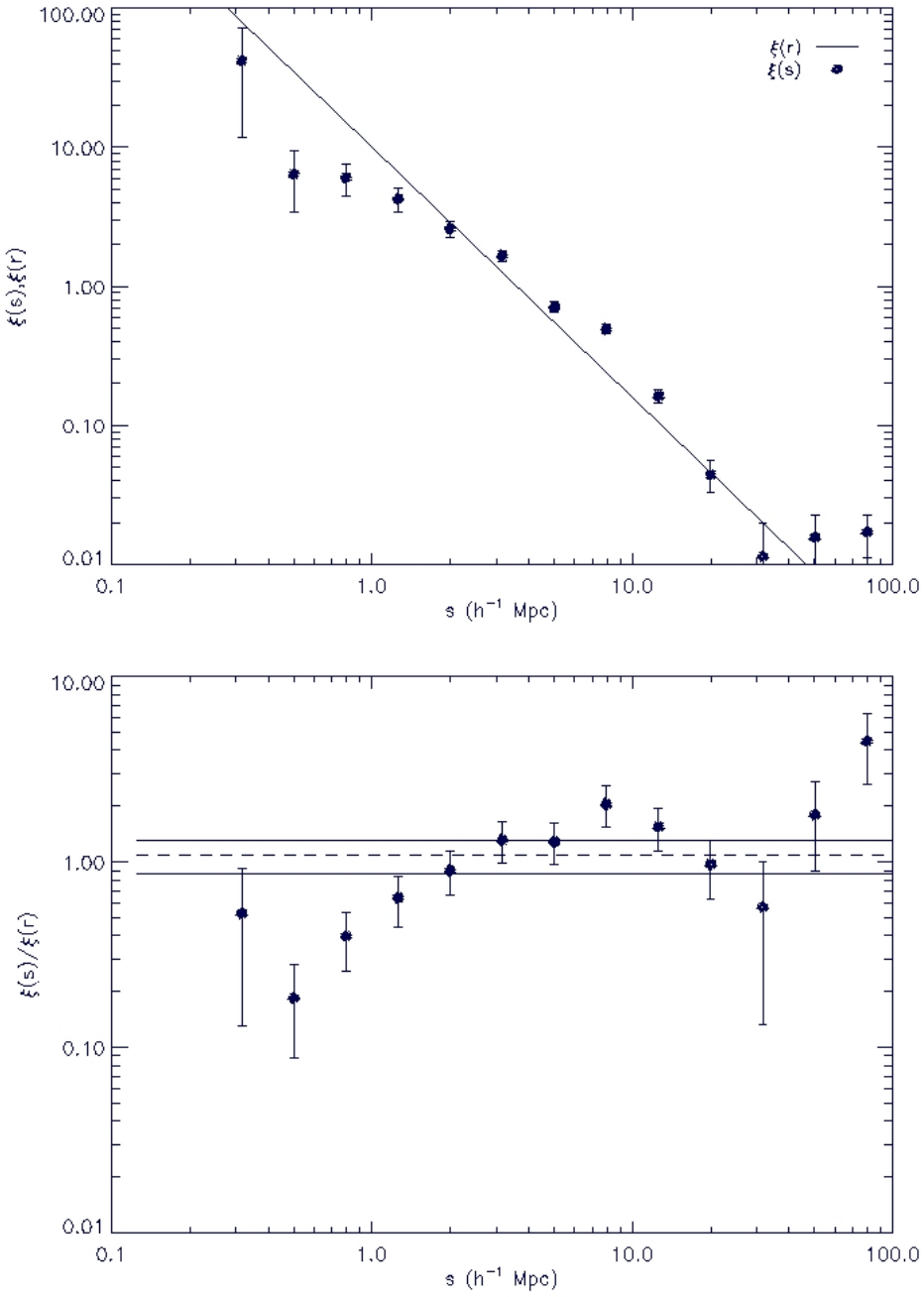

Figure 3.3: a) top: shows $\xi(s)$ from the combined data (Bielby et al. 2008 and Steidel et al. 2003) vs $\xi(r)$, fitted from combined $w_p(\sigma)$ of Bielby et al. 2008 with $\gamma = 1.8$ and $r_0 = 3.63h^{-1}$ Mpc. b) bottom : shows $\xi(s)/\xi(r)$as a function of separation, s.

$$\frac{\xi(s)}{\xi(r)} = (1 + \frac{2}{3}\beta + \frac{1}{5}\beta^2) \quad (3.3)$$

where $\beta \approx \Omega_m^{0.6}/b$

$\xi(r)$ is obtained from Bielby et al. (2008) which has a power-law, $\xi(r) = (\frac{r}{r_0})^{-\gamma}$, with $r_0 = 3.63^{+0.47}_{-0.61} h^{-1} Mpc$ and $\gamma = 1.80$. They obtained r_0 and γ by measuring the projected correlation function, $w_p(\sigma)$ for the combined data.

$\xi(s)$ vs $\xi(r)$ and $\xi(s)/\xi(r)$ as a function of separation is shown in Figure 3.3. The $\xi(s)$ is calculated from the LBG combined data. $\xi(r)$ is fitted from the combined $w_p(\sigma)$ of Bielby et al. 2008 with $\gamma = 1.8$ and $r_0 = 3.63h^{-1}$ Mpc. The error bars are calculated by combining in quadrature the $\xi(s)$ and $\xi(r)$ errors. At the scale $10h^{-1}Mpc$, the z-space contribution is mostly only affected by $\beta(z)$, the gravitational infall (da Angela, 2005). Then we used 4 points of $\xi(s)/\xi(r)$ at large scales between 10 - 40 h^{-1} Mpc to apply a χ^2 fit. In Figure 3.3, the dashed line shows the best fit of $\xi(s)/\xi(r)$. The region between the dashed lines is the 1σ confidence interval in the fit. This fit produces an infall parameter of $\beta = 0.14^{+0.09}_{-0.05}$ at $z = 3$. We then have bias factor, $b \approx \frac{\Omega_m^{0.6}}{\beta} \approx 6.8$.

3.6 Conclusions

We have measured the LBG-LBG correlation functions by using LBG data from VLT and Keck. The total VLT data is 1109 LBGs at $2 < z < 3.5$. We also included 813 LBGs at redshift $2.67 \leq z \leq 3.25$ from Steidel et al. (2003) Keck samples. First, we considered $\xi(s)$ from the VLT data only. Our calculation shows agreement with that of Bielby et al. (2008) from the same data. We have used some updated redshift estimates and this might cause the lower clustering below $8h^{-1}$ Mpc compared to Bielby et al. (2008). We then compared LBG-LBG $\xi(s)$ from Keck data with the $\xi(s)$ fit from da Angela et al. 2005 who used the Steidel et al. (2003) LBG samples. We see lower clustering at the distance below $3h^{-1}$ Mpc but higher clustering at the distance $> 3h^{-1}$ Mpc. This

difference is possibly caused by the estimator that we used to calculate $\xi(s)$. We use the simple form of estimator, $\xi(s) = \frac{Nr}{Ng}\frac{<DD(s)>}{<DR(s)>} - 1$, while da Angela et al. (2005) used the Landy-Szalay estimator. Finally, we compared our VLT result with Keck result. We see lower clustering from the VLT sample at scales $< 10h^{-1}$ Mpc. The error bars from VLT results are higher than in Keck. It is possible that our higher redshift errors may contribute to this difference. We tested the effect of redshift errors by using the $z-$space distortions model from da Angela et al. (2005) by assuming $\gamma = 1.8$, $r_0 = 3.63h^{-1}$ Mpc, $\beta = 0.2$, and $< w_z^2 >^{\frac{1}{2}} = 650kms^{-1}$. We applied the same $z-$space distortions model to the Keck LBG data with a different set of parameters, $\gamma = 1.76$, $r_0 = 4.48h^{-1}$ Mpc, $\beta = 0.25$, and $< w_z^2 >^{\frac{1}{2}} = 530kms^{-1}$. Then we used the combined data from VLT and Keck to calculate LBG-LBG $\xi(s)$. The result from the combined data is consistent with the $\xi(s)$ from da Angela et al. (2005), where $\gamma = 1.71$ and $s_0 = 5.1$ h^{-1} Mpc. We also used the $z-$space distortions model from da Angela et al. (2005) to see the peculiar velocity effects in $\xi(s)$ correlation function. We employed this model by using $\gamma = 1.8$, $r_0 = 3.63h^{-1}$ Mpc, $\beta = 0.2$, and $< w_z^2 >^{\frac{1}{2}} = 590kms^{-1}$. Comparing the VLT and the combined data, we see less effects of the peculiar velocity in the combined data. This is because of the better redshift estimation in Steidel et al. (2003). We also estimated the infall parameter, β at $z = 3$ by using the power-law $\xi(r)$ fitted from the combined $w_p(\sigma)$ of Bielby et al. (2008) and the $\xi(s)$ measurements from combined LBG data. By computing and fitting $\xi(s)/\xi(r)$, we get $\beta = 0.14^{+0.09}_{-0.05}$ at $z = 3$ which gives bias factor $b = 6.8$. This result agrees with Bielby et al. (2008) who get $\beta = 0.21^{+0.13}_{-0.12}$ which was estimated by fitting the power-law $\xi(r)$ to the measurement of $\xi(\sigma, \pi)$.

Chapter 4

Interaction between galaxies and the IGM at $z \sim 3$

4.1 Introduction

In this chapter, we aim to (a) investigate the effect of feedback on the LBG-Lyα cross correlation, (b) also look at metal lines in the QSO spectra. We also want to compare the LBG-CIV cross-correlation with LBG-LBG $\xi(s)$ to see if they are distributed like LBG.

4.2 The connection between LBGs and QSO Absorption Lines

Lyman-break galaxies are used as a powerful tool to study the galaxy-IGM interaction. By considering the cross-correlation between Lyα-LBG and CIV-LBG, we can study the effect of the feedback mechanism on large-scale structure evolution and galaxy formation (da Angela, 2005). The mechanisms of supernova feedback and galactic winds, seem to be the main reason for the enrichment in IGM (Kawata, 2007). The IGM may be heated by galactic winds and accelerated to high velocities. Many models need feedback to regulate the star formation activity (Bielby, 2008) and also limit the number of low-mass galaxies that are produced (Theuns, 2002).

Based on Adelberger's (2003 and 2005) observations, the proximity effect, the lack of

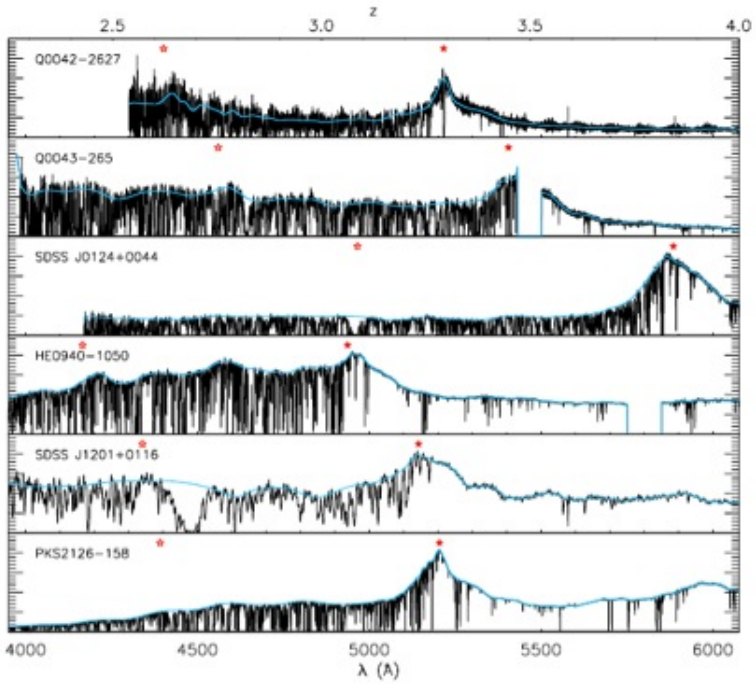

Figure 4.1: (from Bielby, 2008): the VLT UVES, the Keck and the SDSS spectra of 6 bright QSOs. The observed spectra are shown as the black line and the continuum level is indicated by the blue line. The open red stars are the wavelengths of the intrinsic Lyβ while the filled red stars are the wavelengths of the intrinsic Lyα.

Lyα absorption near the background QSO, is still an open question. It is still unclear whether galactic winds have effects on the galaxy and its surroundings or not. This motivation from the results of Adelberger et al. (2003, 2005) leads us to try to extend their work on the correlation between QSO absorption and LBGs at high redshift by using VLT LBG data from Bielby et al. (2008). Here we reanalyze the results of Bielby et al. (2008) by using different methods and error analysis.

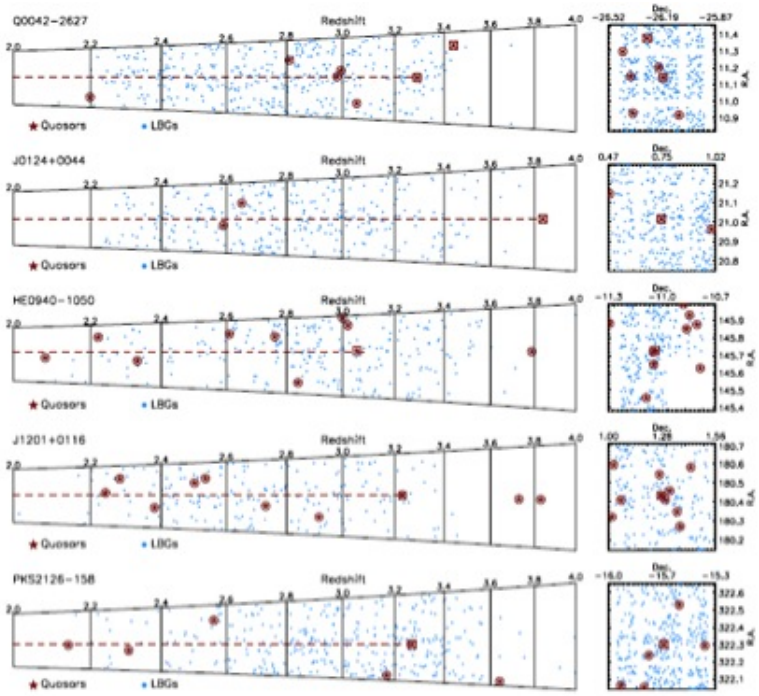

Figure 4.2: (from Bielby, 2008): shows the LBG distributions of five fields; Q0042-2627, J0124+0044, HE0940-1050, J1201+0116 and PKS2126- 58, in R.A., Declination and redshift. The blue filled circles are the spectroscopically confirmed LBGs and the dark red stars are the known QSOs. The red stars are the QSOs with the low-resolution spectra from VLT VIMOS and AAT AAOmega and the red crosses are the medium-resolution spectra from SDSS J1201+0116. The red squares represent QSOs with high-resolution spectra from VLT UVES, Keck HIRES.

Name	R.A.	Dec	z	Facility
Q0042-2627	11.1414583	-26.1888611	3.29	Keck
$[WH09]0043-265$	11.3769999	-26.2860546	3.45	Keck
SDSS J0124+0044	21.0157089	0.7424445	3.83	UVES
HE0940-1050	145.722500	-11.0736113	3.06	UVES
SDSS J1201+0116	180.434880	1.2698889	3.23	SDSS
PKS2126-158	322.300625	-15.644674	3.27	UVES

Table 4.1: (from Bielby, 2008): Bright QSOs with high resolution spectra from the facilities listed.

4.3 QSO Lyα - LBG cross correlation

4.3.1 Observational data

High Resolution QSO Spectra

We use the data from Bielby et al. (2008), who obtained 5 high resolution spectra from bright QSOs and a medium resolution spectrum as summarised in Table 4.1. Three QSOs, SDSS J0124+0044, HE0940-1050 and PKS2126-158, were taken by using Ultraviolet and Visual Echelle Spectrograph (UVES). A medium resolution spectrum of SDSS J1201+0116 is taken from the Sloan Digital Sky Survey (SDSS). $[WH09]0043-265$ and Q0042-2627 are obtained by Keck/HIRES. The observed spectra from 6 bright QSOs are shown in Figure 4.1. The LBG data used in this calculation are described in Chapter 3. Figure 4.2 shows the distributions of LBGs that are located around five fields of bright QSOs.

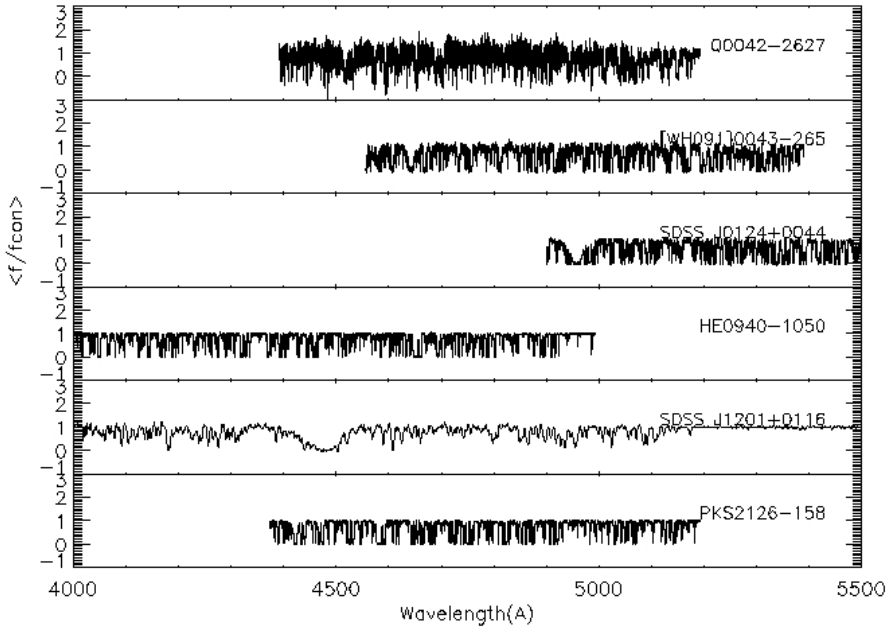

Figure 4.3: Transmissivity $< \frac{f}{f_{con}} >$ of the Lyα forest measured in the high-resolution spectra of 6 bright QSOs.

Low Resolution QSO Spectra

We use a combination of QSO data from the 6 QSO high-resolution spectra and 22 low-resolution spectra. In total, we have 28 QSOs data from Bielby et al. (2008) as detailed in Table 4.2 to calculate cross-correlation for low-resolution spectra. The QSOs spectra are obtained from several measurements. As mentioned before the high-resolution QSOs are from UVES, SDSS, and Keck/HIRES. The low-resolution QSOs that lie within 5′ are obtained from the AAOmega instrument at the Anglo-Australian Observatory (AAO). The ′Quasars near Quasars′ (QNQ) survey observed with FORS2 on the VLT are also included.

Name	R.A.	Dec	z	Facility
Q0042-2627	11.14145	-26.18886	3.29	Keck
$[WH09]0043-265$	11.37699	-26.28605	3.45	Keck
LBQS 0041-2638	10.92837	-26.36963	3.05	AAT
SDSS J0124+0044	21.01570	0.74244	3.83	UVES
J012351+005958	20.96249	0.99961	2.59	AAT
HE0940-1050	145.72250	-11.07361	3.06	UVES
J094208-112856	145.53412	-11.48238	2.47	AAT
J094220-112215	145.58362	-11.37105	2.81	AAT
J094252-112707	145.71991	-11.45211	3.16	AAT
J094331-111949	146.00662	-11.33036	2.61	AAT
J094342-105231	145.92912	-10.87544	3.02	AAT
J094349-112800	145.95662	-11.46686	3.48	AAT
J094357-105435	145.99025	-10.90975	3.02	AAT
J094400-112732	146.00154	-11.45908	2.56	AAT
J094407-112632	146.03212	-11.44225	2.83	AAT
J094408-105039	146.03392	-10.84441	2.68	AAT
J09425-1048	145.62740	-10.81413	2.32	FORS2
J09427-1121	145.68512	-11.36080	2.96	FORS2
J09434-1053	145.85092	-10.89249	2.76	FORS2
SDSS J1201+0116	180.43488	1.26988	3.23	SDSS
SDSS J120055.77+013430.7	180.23238	1.57519	2.51	AAT
2QZ J120117.1+010045	180.32124	1.01261	2.38	AAT
SDSS J120210.55+011544.2	180.54396	1.26227	2.50	AAT
SDSS J120222.68+010120.1	180.59450	1.02225	2.28	AAT
SDSS J120138.56+010336.1	180.41066	1.06002	3.86	AAT
PKS2126-158	322.30062	-15.64460	3.27	UVES
J212904-160249	322.27042	-16.04694	2.92	AAT
J21301-1533	322.53110	-15.55580	3.49	FORS2

Table 4.2: Details of high-resolution and low-resolution QSO spectra.

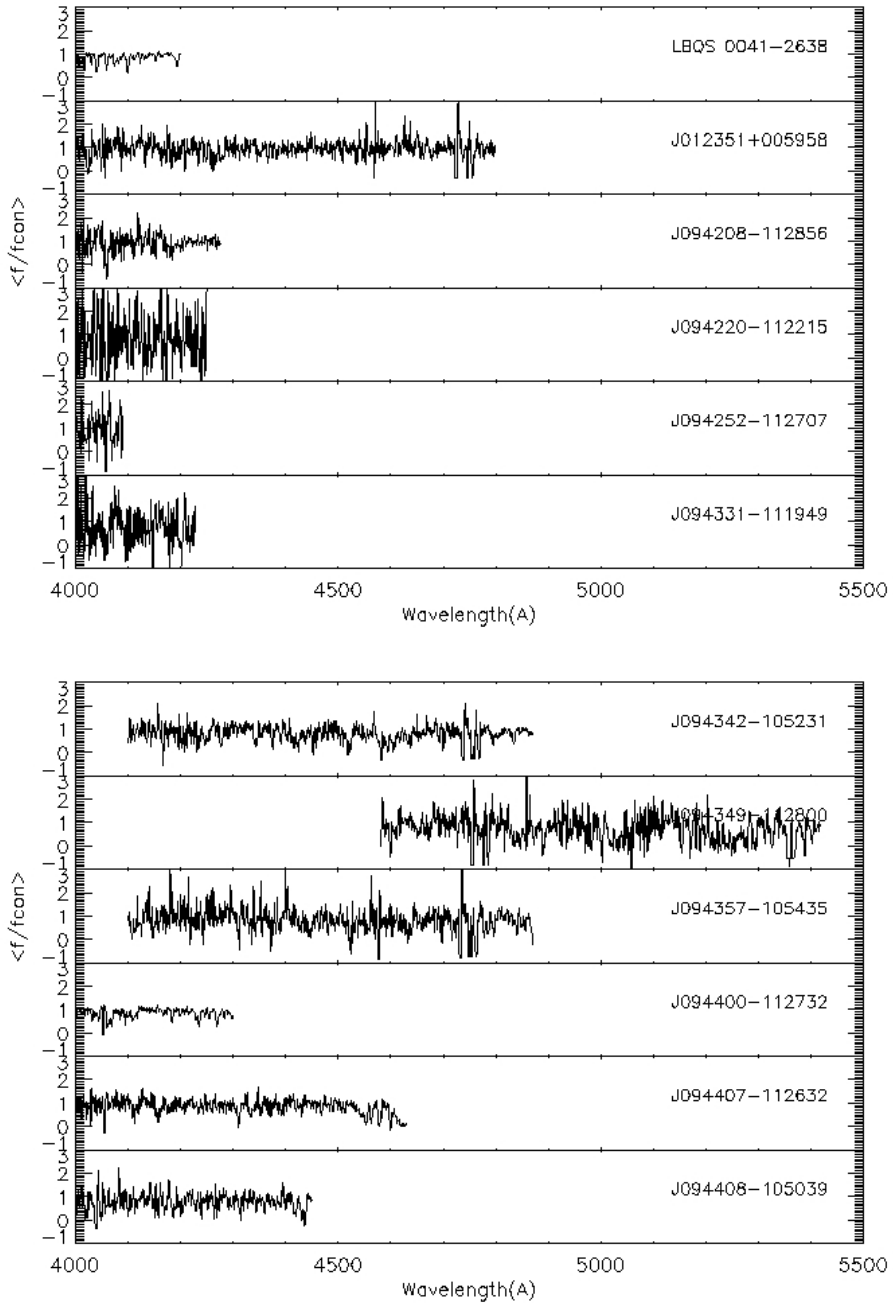

Figure 4.4: Transmissivity $< \frac{f}{f_{con}} >$ of the Lyα forest measured in the low-resolution spectra of 22 bright QSOs.

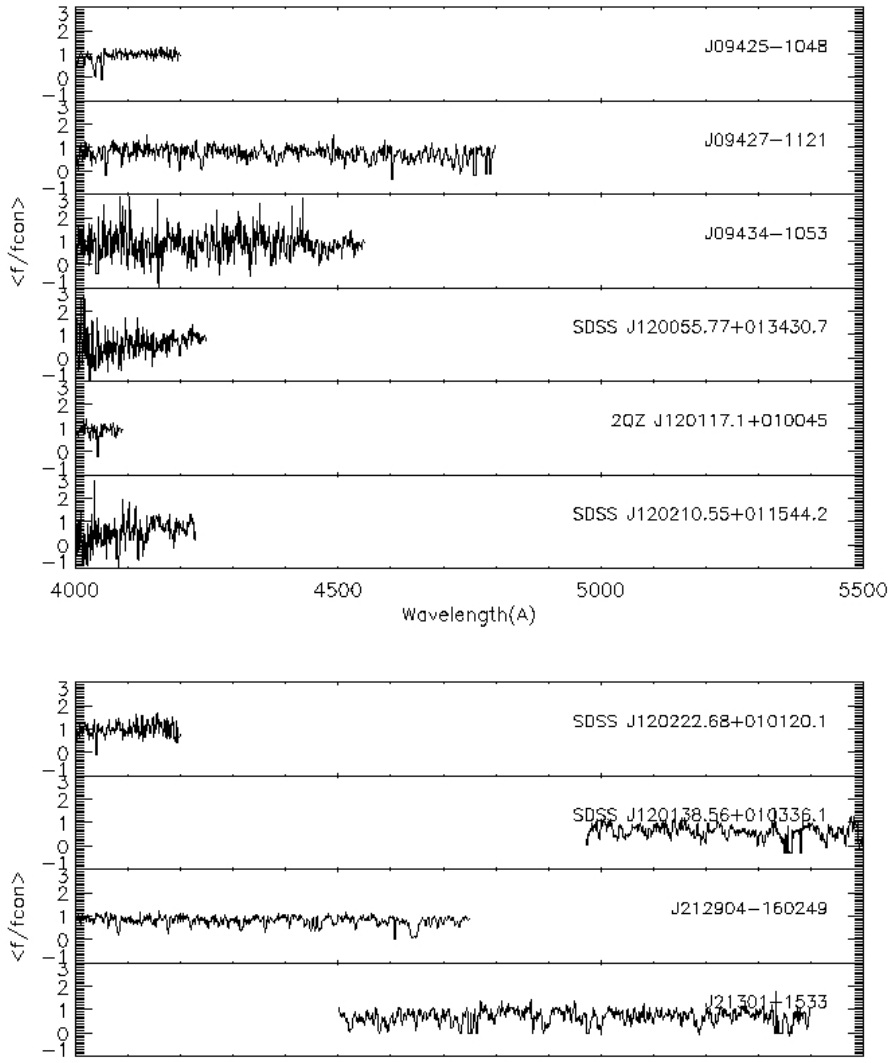

Figure 4.4: Transmissivity $< \frac{f}{f_{con}} >$ of the Lyα forest measured in the low-resolution spectra of 22 bright QSOs

4.3.2 Cross correlation

We use the transmissivity of the Lyα forest to calculate the Ly-LBG cross-correlation function. We use:

$$T = \frac{f}{f_{con}} \tag{4.1}$$

where f is the observed flux and f_{con} is the continuum in flux level from Lyα forest. Then, we have to normalize the QSO transmissivities by using equation (6.2) from Bielby et al. (2008) which was also used by Adelberger et al. (2003).

$$\bar{T} = 0.676 - 0.220(z - 3) \tag{4.2}$$

and

$$T_z = \frac{T}{\bar{T}} \tag{4.3}$$

This normalization is used to correct for the evolution of Lyα transmissivity with redshift since the transmissivity is higher at low redshift.

We follow Bielby's way of selecting data, many conditions need to be set before calculating the cross-correlations. Firstly, we need to avoid the effect of contamination of Lyα absorption lines by cutting out the spectrum below the Lyα emission. The spectrum between the Lyβ and Lyα are only taken into this calculation. Secondly, to prevent the proximity effects from the QSOs, the wavelength within 20 $\mathring{A}$ of the intrinsic Lyα emission are also excluded. Thirdly, the spectrum of J1201+0116 is cut in the range z = 2.69 since it contains a damped Lyλ systems. Finally, we also used S/N = $f_{con}/\sqrt{variance} < 3$ to exclude poor QSO spectra. Figure 4.3 and Figure 4.4 show the transmissivity from high

and low resolution spectra respectively. We used these transmissivity to calculate the Lyα-LBG cross correlation function.

The Lyα-LBG cross correlation function was evaluated from

$$\xi(s) \quad = \quad \frac{< DT(s) >}{N(s)} \tag{4.4}$$

where $< DT(s) >$ is the number of galaxy-Lyα pairs weighted by the normalized transmissivity: T_z, for each separations. N(s) is the number of LBG that contribute in each pairs. This is a different approach from Bielby et al. (2008) and Adelberger et al. (2003) who use a correlation function approach based on the Landy-Szalay estimator.

4.3.3 Error estimators

We have considered three ways to estimate the error on the cross-correlation function:

1. The simplest way is the field-to-field standard error as used by Bielby et al. (2008). The number of DT pairs in each separation are counted. We then obtain a mean value, $\bar{x}$, from DT divided by the number of fields. The standard error for mean value can be defined as: $\alpha = \frac{\sigma_{N-1}}{\sqrt{N}}$ where $\sigma_{N-1} = \sqrt{\frac{\sum_i (x_i - \bar{x})^2}{N-1}}$ is the standard deviation. In this case, $x =< DT >$ and the number of field, N = 6 and 28 for high and low resolution respectively. The problem of this error estimate is the standard deviation is weighted depending on field. It is weighted equally for each field which does not take account of the actual number of LBGs at a given separation.

2. The weighted mean method. Considering the number of pairs in individual fields at the given separations. Then calculate a mean value, $\bar{x}$ and standard error. The results from each field are supposed to be $x_i \pm \alpha_{x_i}$. α_{x_i} is the error calculated by standard

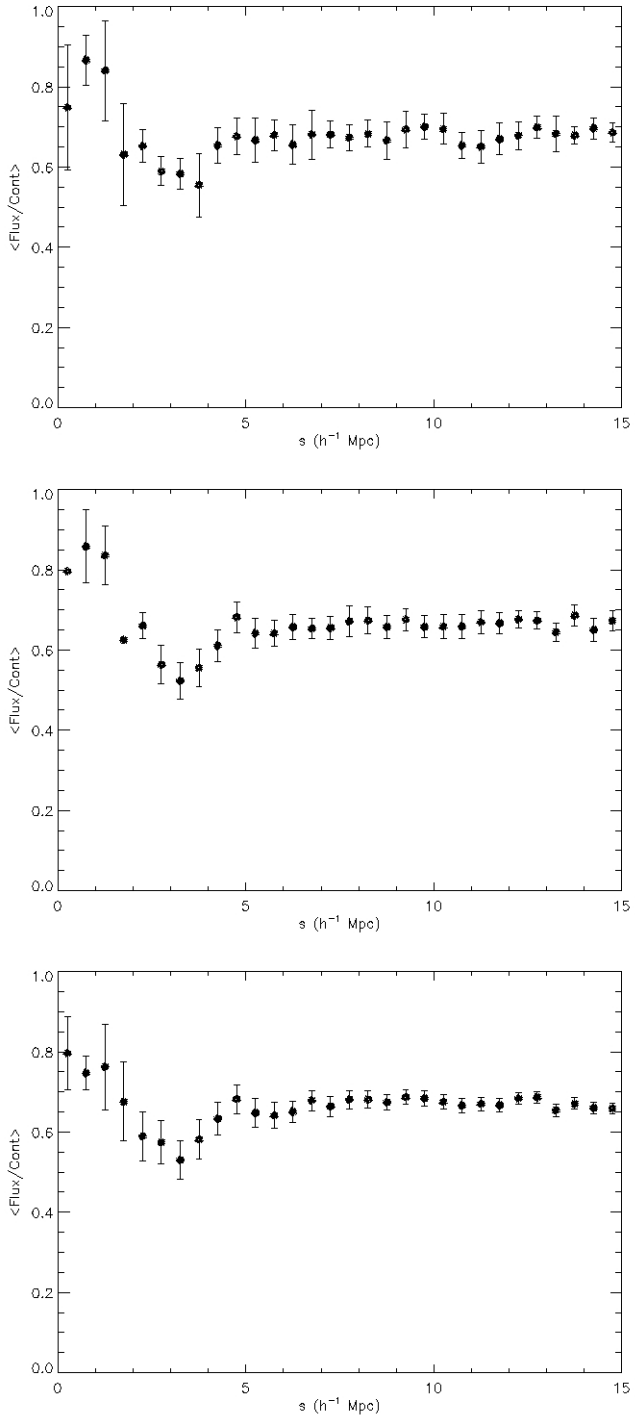

Figure 4.5: The Lyα-LBG $\xi(s)$ error bars calculated by method 1, 2, and 3 respectively.

deviation in each given separation in each fields. The combined estimate of true value is:

$$\bar{x}_{i,j,k,...} = \frac{\sum_i \frac{x_i}{{\alpha_i}^2}}{\sum_i \frac{1}{{\alpha_i}^2}} \tag{4.5}$$

The standard error is:

$$\frac{1}{\alpha^2_{\bar{x}_{i,j,k,...}}} = \sum_i \frac{1}{{\alpha_{x_i}}^2} \tag{4.6}$$

In this case, $x =< DT >$, α_{x_i} is the error calculated from each field, and N is the number of fields that contributed to each bin. This method weights the final average depending on the number of LBG data points that contributes to each bin so there are no account from the fields that gave zero pair. The advantage of this method is instead of using the standard deviation calculated from field-to-field variation which weights each field the same, no matter how many LBGs at a given separation, now we calculate by the weighted-error method which depends on the actual number of LBGs per field and in each bin. The problem of this error estimator is the small number of LBG in the inner bin. We only have 2 LBGs in the first separation bin from different field and this makes it impossible to obtain α_{x_i} from only 1 LBG.

3. The LBG-LBG error. At each bin, DT are added from all the Lyα transmissivity pixels and LBGs. To get the average value of $< DT >$, the summation of DT in each bin was divided by the number of LBGs. We then used the standard deviation from LBG-LBG variation which depends on the different numbers of overall LBGs in a bin to calculate the error bar. That is:

$$\Delta\xi(s) = \frac{1}{\sqrt{N}} \sqrt{\frac{\sum_i (x_i - \bar{x})^2}{N-1}} \tag{4.7}$$

where x= DT, $\bar{x}$ =< DT > and N is the number of LBGs in each bin. This gets rid of the problem of lower numbers of LBGs in the smallest separation bin in the previous method.

Figure 4.5 shows the error bars calculated from three methods. Since the LBG-LBG error method seems to give the best errors particularly at small scales, then generally our errors will be based on this LBG-LBG error.

4.3.4 Results

From our results Figure 4.6, we present the LBG-Lyα transmissivity correlation function compared to the results from Adelberger et al. (2003 and 2005). Bielby et al. (2008) obtained 6 QSO sightlines with high resolution spectroscopy from VLT VIMOS LBG Survey. The filled circles illustrate VLT VIMOS LBG Survey. The open diamonds show the results of Adelberger et al. (2003) and Adelberger et al. (2005) in Figure 4.6 (a) and Figure 4.6 (b), respectively. Our bin size is 0.5 h^{-1} Mpc and the error bars are calculated by LBG-LBG error method. At distances greater than 3 h^{-1} Mpc, we found agreement with both Adelberger et al. (2003 and 2005). The measured $< flux/cont >$ increases with separation and reaches the mean value at $< flux/cont > \approx 0.65$. At separations below 3 h^{-1} Mpc, our results seem to have the same trend as Adelberger et al. (2003). At $s < 0.5h^{-1}$ Mpc from LBGs , we found a decrease in H_I density like Adelberger et al. (2003). However, there are only 2 LBGs at that separation.

Since we have small number of LBGs at distances within 3 h^{-1} Mpc, we are looking for more QSO sightlines which may contribute more pairs at small separations from galaxies. We therefore combined high and low resolution spectra and employed the same method applied to obtain Lyα-LBG $\xi(s)$ from 6 QSOs to calculate $\xi(s)$ from 28 QSO spectra. The results from the combined QSOs sightlines are shown in Figure 4.7. Similar to Figure 4.6,

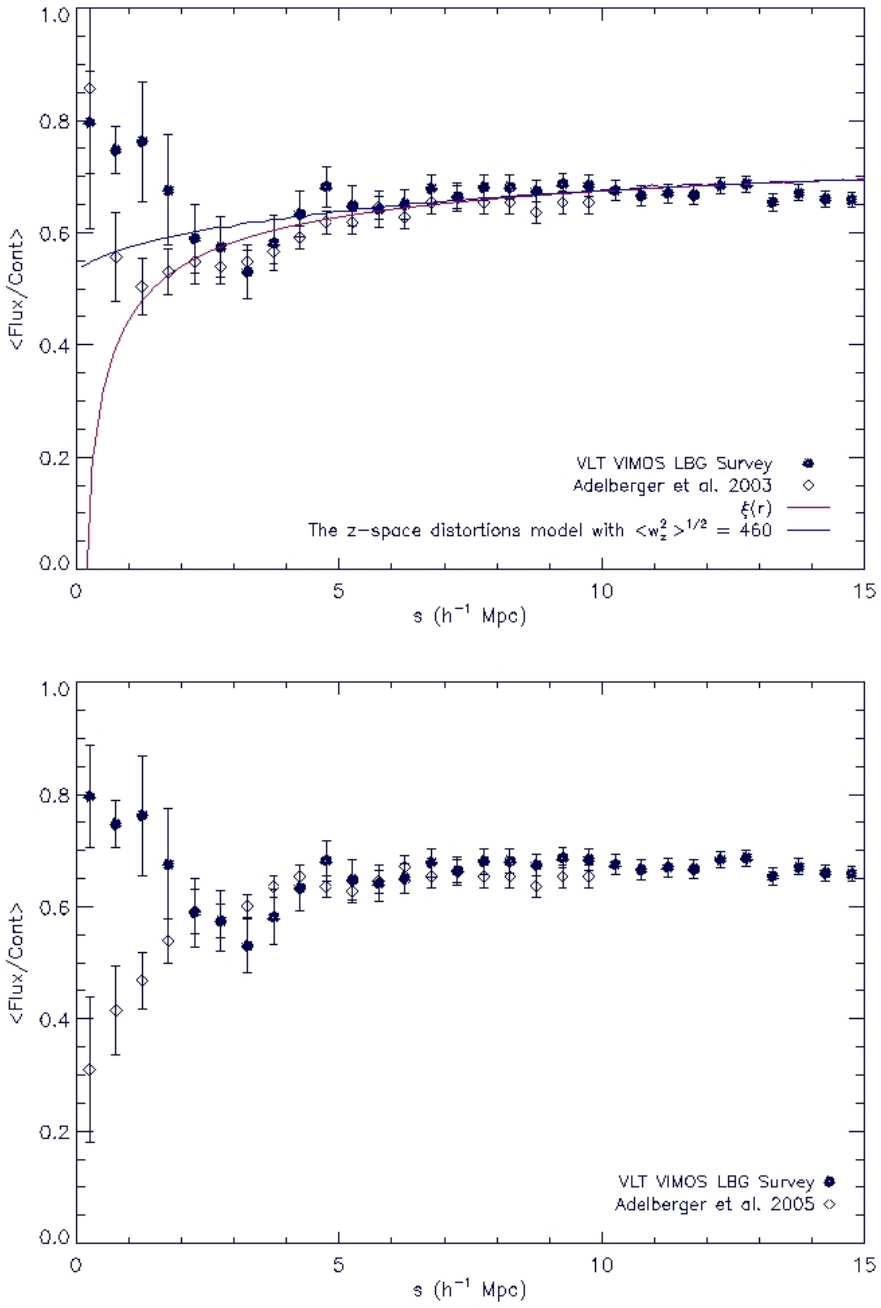

Figure 4.6: The Lyα transmissivity-LBG correlation from 6 QSO sightlines with high resolution spectroscopy from VLT VIMOS LBG Survey. a) top: shows the comparison with Adelberger et al. (2003). The pink solid line shows $\xi(r)$ fitted to the simulation in Figure 5.6 (c), with $\gamma = 0.45$ and $r_0 = 0.1h^{-1}$ Mpc. The blue solid line is the $z-$space distortions model from da Angela et al. (2005), here assuming $\gamma = 0.45$, $r_0 = 0.1h^{-1}$ Mpc, $\beta = 0.2$, and $< w_z^2 >^{\frac{1}{2}} = 460 kms^{-1}$.b) bottom: shows the comparison with Adelberger et al. (2005).

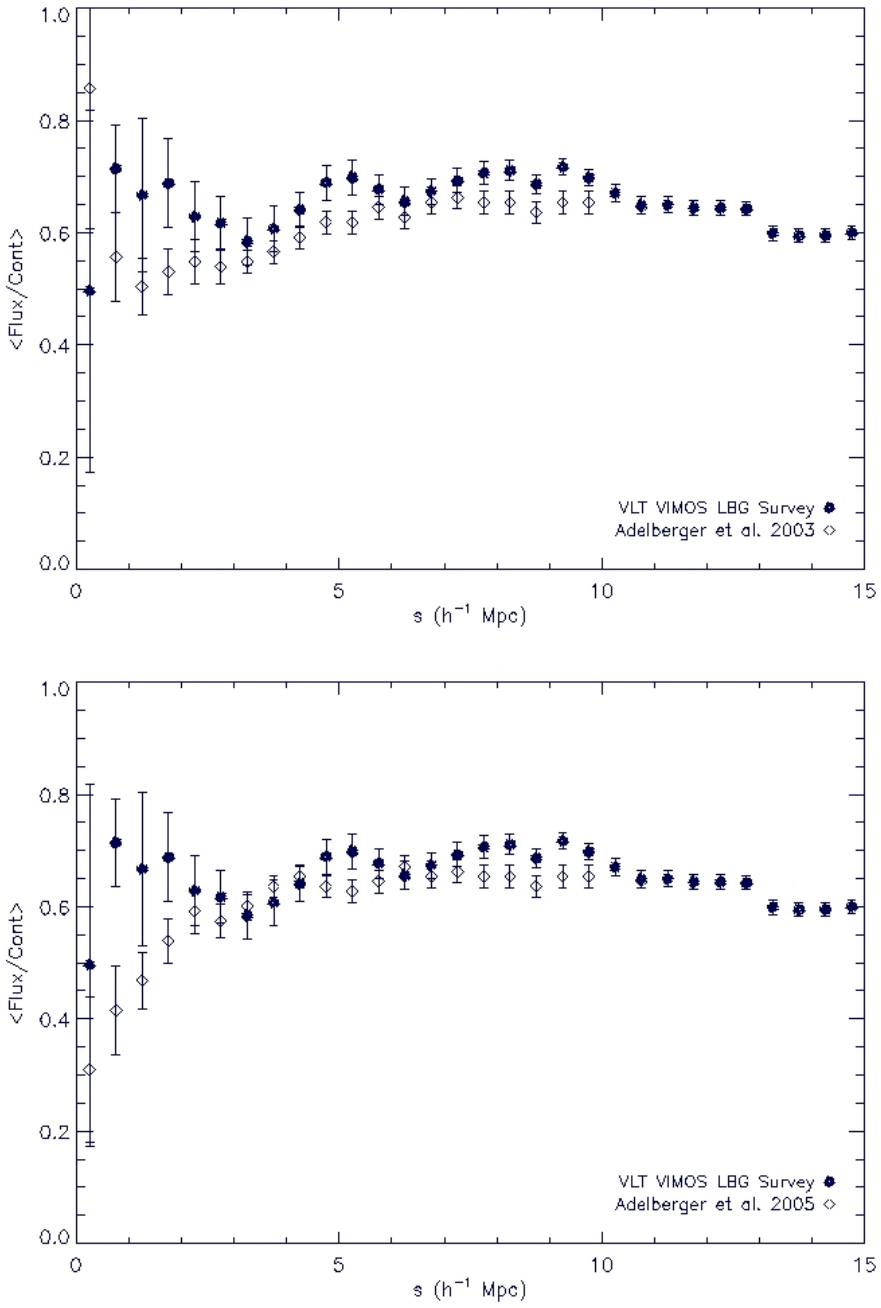

Figure 4.7: The Lyα transmissivity-LBG correlation from 28 QSO sightlines a) top: shows the comparison with Adelberger et al. (2003). b) bottom: shows the comparison with Adelberger et al. (2005).

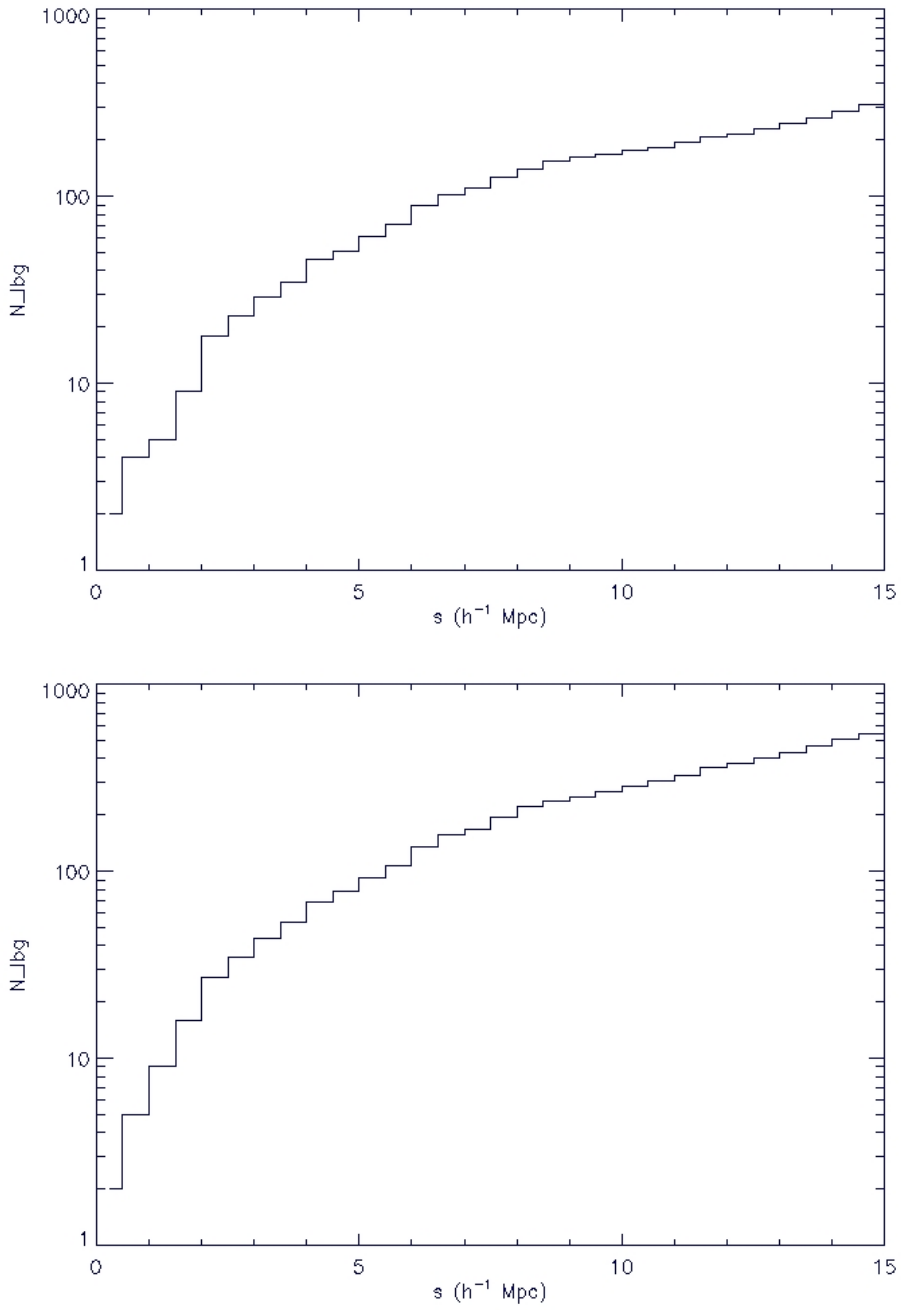

Figure 4.8: a) top and b) bottom : The number of LBGs in each separation which contribute to 6 QSO and 28 QSO sightlines calculation, respectively.

our result from 28 QSOs is compared to the results of Adelberger et al. (2003) and Adelberger et al. (2005) in Figure 4.7 (a) and Figure 4.7 (b), respectively. Here, we found similar trends with the results from only 6 QSOs with high-resolution spectra.

The number of LBGs that contribute to each bin are presented in Figure 4.8 (a) and (b) for the 6 QSO and 28 QSO calculation respectively. We still have only 2 LBGs in the first bin and we have no additional LBG from low-resolution spectra to this bin. The low resolution QSO spectra have only a small effect on the number of LBGs that contribute to small separations.

We have checked the effect of using the velocity dispersions fitted to the LBG-LBG $\xi(s)$ to smooth the real space $\xi(r)$ to obtain the $z-$space $\xi(s)$ in Figure 4.6 (a). The pink solid line shows a power law fitted with $\gamma = 0.45$ and $r_0 = 0.1h^{-1}$ Mpc to the simulation in Figure 5.6 (c) below as a representation of the real-space cross-correlation function. The blue solid line is an estimation of the $z-$space cross-correlation function based on the real-space fit and the $z-$space distortion model of da Angela et al. (2005), with velocity dispersions of $< w_z^2 >^{\frac{1}{2}} = \frac{650}{\sqrt{2}} = 460 kms^{-1}$. Since $460 kms^{-1}$ correspond to 4-5 comoving Mpc at $z = 3$, we confirm that the smoothing effect of the velocity dispersions is quite large at small scales and this will need to be taken into account in any future detailed interpretation of these data. The question of the strength of the feedback we see in the data will also be affected by this velocity smoothing but we leave this for later work.

4.4 QSO CIV- LBG cross correlation

Observing the metal absorption from QSO spectra in the Lyman alpha forest allow us to investigate the impact of feedback on the intergalactic medium. Adelberger et al. (2005) found that CIV and LBG are in the same part of the Universe and they are suggested to be the same systems. They found a similar result for the LBG-CIV cross-correlation function and the LBG-LBG auto-correlation function. These findings also inspired us to extend their work on the CIV-LBG cross-correlation function.

4.4.1 Observational data

The data used in the calculation are from Crighton et al. (2009, in preparation). The CIV systems are contained from AAOmega, Williger, UVES and HIRES spectra. Multiple systems are often observed in QSOs with the highest S/N and resolution spectra. In total, we have 176 CIV systems from 60 QSOs as shown in Table 4.3. The summarized details are shown in Table 4.3. Note that ew. stands for equivalent width.

4.4.2 Correlation function

The correlation function of LBG-CIV is calculated by

$$\xi(s) \quad = \quad \frac{Nr}{Ng} \frac{< D_{CIV} D_{LBG}(s) >}{< D_{CIV} R_{LBG}(s) >} - 1 \tag{4.8}$$

where $< D_{CIV} D_{LBG}(s) >$ is the average number of pairs of CIV systems and LBG data. $< D_{CIV} R_{LBG}(s) >$ is the number of pairs of CIV system and random LBGs at the separation s. The factor Nr/Ng is the ratio of the number of random and data points.

The error estimate on $\xi(s)$ is calculated by Poisson error estimates, which is defined as:

$$\Delta\xi(s) = \frac{1 + \xi(s)}{\sqrt{< D_{CIV} D_{LBG}(s) >}} \tag{4.9}$$

4.4.3 Results

The results of the CIV-LBG correlation from VLT survey is shown in Figure 4.9. CIV-LBG $\xi(s)$ and LBG-LBG $\xi(s)$ are presented by filled circles and open diamonds respectively.

QSO name	RA	Dec	z (QSO)	z (CIV doublet)	ew
TS0417	145.6850	-11.3607	2.960	2.488	2.669
TS0417	145.6850	-11.3607	2.960	2.892	2.587
MC065102	145.9566	-11.4668	3.480	2.566	4.665
MC065102	145.9566	-11.4668	3.480	2.578	2.652
MC065102	145.9566	-11.4668	3.480	3.135	2.440
TS0292	145.6272	-10.8141	2.330	1.854	0.923
TS0292	145.6272	-0.8141	2.330	2.321	0.509
MC068682	146.0015	-11.4590	2.558	1.864	0.344
MC068682	146.0015	-11.4590	2.558	1.880	0.658
MC068682	146.0015	-11.4590	2.558	1.947	1.321
MC068682	146.0015	-11.4590	2.558	2.186	0.931
MC068682	146.0015	-11.4590	2.558	2.340	0.840
MC394567	146.0339	-10.8444	2.680	2.254	2.033
MC071514	145.7199	-11.4521	3.147	2.975	3.904
MC071514	145.7199	-11.4521	3.147	3.129	1.034
MC077364	146.0321	-11.4422	2.832	2.811	1.717
MC077364	146.0321	-11.4422	2.832	2.827	0.967
HE0940-1050	145.7229	-11.0738	3.054	2.220	0.991
HE0940-1050	145.7229	-11.0738	3.054	2.330	3.061
HE0940-1050	145.7229	-11.0738	3.054	2.408	0.357
HE0940-1050	145.7229	-11.0738	3.054	2.516	0.082
HE0940-1050	145.7229	-11.0738	3.054	2.613	0.057
HE0940-1050	145.7229	-11.0738	3.054	2.643	0.218
HE0940-1050	145.7229	-11.0738	3.054	2.667	0.641

Table 4.3: details of CIV systems

QSO name	RA	Dec	z (QSO)	z (CIV doublet)	ew
HE0940-1050	145.7229	-11.0738	3.054	2.825	0.678
HE0940-1050	145.7229	-11.0738	3.054	2.826	1.629
HE0940-1050	145.7229	-11.0738	3.054	2.834	1.620
HE0940-1050	145.7229	-11.0738	3.054	2.860	0.085
HE0940-1050	145.7229	-11.0738	3.054	2.916	0.346
HE0940-1050	145.7229	-11.0738	3.054	2.937	0.133
HE0940-1050	145.7229	-11.0738	3.054	3.038	0.091
213054.400-160540	322.7266	-16.0945	2.578	2.230	5.384
212904.900-160249	322.2704	-16.0469	2.905	2.149	0.091
212904.900-160249	322.2704	-16.0469	2.905	2.163	3.747
212904.900-160249	322.2704	-16.0469	2.905	2.356	0.474
212904.900-160249	322.2704	-16.0469	2.905	2.436	0.250
212904.900-160249	322.2704	-16.04694	2.905	2.823	0.375
212904.900-160249	322.2704	-16.0469	2.905	2.847	0.652
[HB89]-2126-158	322.3006	-15.6446	3.268	2.394	1.662
[HB89]-2126-158	322.3006	-15.6446	3.268	2.459	0.316
[HB89]-2126-158	322.3006	-15.6446	3.268	2.485	0.086
[HB89]-2126-158	322.3006	-15.6446	3.268	2.553	0.161
[HB89]-2126-158	322.3006	-15.6446	3.268	2.637	2.277
[HB89]-2126-158	322.3006	-15.6446	3.268	2.678	0.695
[HB89]-2126-158	322.3006	-15.6446	3.268	2.727	0.371
[HB89]-2126-158	322.3006	-15.6446	3.268	2.768	3.366
[HB89]-2126-158	322.3006	-15.6446	3.268	2.819	0.590
[HB89]-2126-158	322.3006	-15.6446	3.268	2.907	0.543
[HB89]-2126-158	322.3006	-15.6446	3.268	2.963	0.313

QSO name	RA	Dec	z (QSO)	z (CIV doublet)	ew
[$HB89$]-2126-158	322.3006	-15.6446	3.268	2.967	0.354
[$HB89$]-2126-158	322.3006	-15.6446	3.268	3.098	0.021
[$HB89$]-2126-158	322.3006	-15.6446	3.268	3.216	0.298
J21301-1533	322.5310	-15.5558	3.463	2.545	0.964
J21301-1533	322.5310	-15.5558	3.463	3.113	1.851
J21301-1533	322.5310	-15.5558	3.463	3.266	1.498
nbc012351+005958	20.9625	0.9996	2.590	2.510	2.154
SDSS-J0124+0044	21.0157	0.7424	3.807	2.833	0.876
SDSS-J0124+0044	21.0157	0.7424	3.807	2.866	0.081
SDSS-J0124+0044	21.0157	0.7424	3.807	2.910	0.701
SDSS-J0124+0044	21.0157	0.7424	3.807	2.942	0.110
SDSS-J0124+0044	21.0157	0.7424	3.807	2.986	1.943
SDSS-J0124+0044	21.0157	0.7424	3.807	3.065	1.500
SDSS-J0124+0044	21.0157	0.7424	3.807	3.148	0.114
SDSS-J0124+0044	21.0157	0.7424	3.807	3.187	0.135
SDSS-J0124+0044	21.0157	0.7424	3.807	3.000	1.186
SDSS-J0124+0044	21.0157	0.7424	3.807	3.548	1.793
SDSS-J0124+0044	21.0157	0.7424	3.807	3.673	2.420
SDSS-J0124+0044	21.0157	0.7424	3.807	3.765	0.660
SDSS-J12013+0103	180.4106	1.0600	3.839	3.794	5.871
2QZ-J120117+01004	180.3213	1.0127	2.380	1.656	2.675
2QZ-J120117+01004	180.3213	1.0127	2.380	2.041	1.125
SDSS-J12014+01161	180.4348	1.2699	3.202	2.515	0.560
SDSS-J12014+01161	180.4348	1.2699	3.202	2.651	0.253
SDSS-J12014+01161	180.4348	1.2699	3.202	2.665	0.855

QSO name	RA	Dec	z (QSO)	z (CIV doublet)	ew
SDSS-J12014+01161	180.4348	1.2699	3.202	2.683	1.293
SDSS-J12014+01161	180.4348	1.2699	3.202	2.788	0.453
LBQS-0042-2627	11.1414	-26.1888	3.289	2.474	0.998
LBQS-0042-2627	11.1414	-26.1888	3.289	2.506	0.281
LBQS-0042-2627	11.1414	-26.1888	3.289	2.728	0.421
LBQS-0042-2627	11.1414	-26.1888	3.289	2.778	0.108
LBQS-0042-2627	11.1414	-26.1888	3.289	2.827	0.288
LBQS-0042-2627	11.1414	-26.1888	3.289	3.101	0.538
LBQS-0042-2627	11.1414	-26.1888	3.289	3.144	0.389
LBQS-0042-2627	11.1414	-26.1888	3.289	3.212	0.272
LBQS-0042-2627	11.1414	-26.1888	3.289	3.235	0.843
LBQS-0041-2638	10.9282	-26.3695	3.053	2.264	1.036
LBQS-0041-2638	10.9282	-26.3695	3.053	2.338	0.618
LBQS-0041-2638	10.9282	-26.3695	3.053	2.568	0.800
LBQS-0041-2638	10.9282	-26.3695	3.053	2.739	1.410
LBQS-0041-2638	10.9282	-26.3695	3.053	2.000	0.000
[WH091]-0043-265	11.3769	-26.2858	3.440	2.719	0.201
[WH091]-0043-265	11.3769	-26.2858	3.440	2.818	2.061
[WH091]-0043-265	11.3769	-26.2858	3.440	3.044	3.086
[WH091]-0043-265	11.3769	-26.2858	3.440	3.120	0.881
[WH091]-0043-265	11.3769	-26.2858	3.440	3.129	0.401
[WH091]-0043-265	11.3769	-26.2858	3.440	3.153	0.180
[WH091]-0043-265	11.3769	-26.2858	3.440	3.254	1.255
SDSS-J12014+01161	180.4348	1.2699	3.202	2.683	1.293
SDSS-J12014+01161	180.4348	1.2699	3.202	2.788	0.453
LBQS-0042-2627	11.1414	-26.1888	3.289	2.474	0.998
LBQS-0042-2627	11.1414	-26.1888	3.289	2.506	0.281
LBQS-0042-2627	11.1414	-26.1888	3.289	2.728	0.421

QSO name	RA	Dec	z (QSO)	z (CIV doublet)	ew
LBQS-0042-2627	11.1414	-26.1888	3.289	2.778	0.108
LBQS-0042-2627	11.1414	-26.1888	3.289	2.827	0.288
LBQS-0042-2627	11.1414	-26.1888	3.289	3.101	0.538
LBQS-0042-2627	11.1414	-26.1888	3.289	3.144	0.389
LBQS-0042-2627	11.1414	-26.1888	3.289	3.212	0.272
LBQS-0042-2627	11.1414	-26.1888	3.289	3.235	0.843
LBQS-0041-2638	10.9282	-26.3695	3.053	2.264	1.036
LBQS-0041-2638	10.9282	-26.3695	3.053	2.338	0.618
LBQS-0041-2638	10.9282	-26.3695	3.053	2.568	0.800
LBQS-0041-2638	10.9282	-26.3695	3.053	2.739	1.410
LBQS-0041-2638	10.9282	-26.3695	3.053	2.000	0.000
[WH091]-0043-265	11.3769	-26.2858	3.440	2.719	0.201
[WH091]-0043-265	11.3769	-26.2858	3.440	2.818	2.061
[WH091]-0043-265	11.3769	-26.2858	3.440	3.044	3.086
[WH091]-0043-265	11.3769	-26.2858	3.440	3.120	0.881
[WH091]-0043-265	11.3769	-26.2858	3.440	3.129	0.401
[WH091]-0043-265	11.3769	-26.2858	3.440	3.153	0.180
[WH091]-0043-265	11.3769	-26.2858	3.440	3.254	1.255
[WH091]-0043-265	11.3769	-26.2858	3.440	3.371	0.452

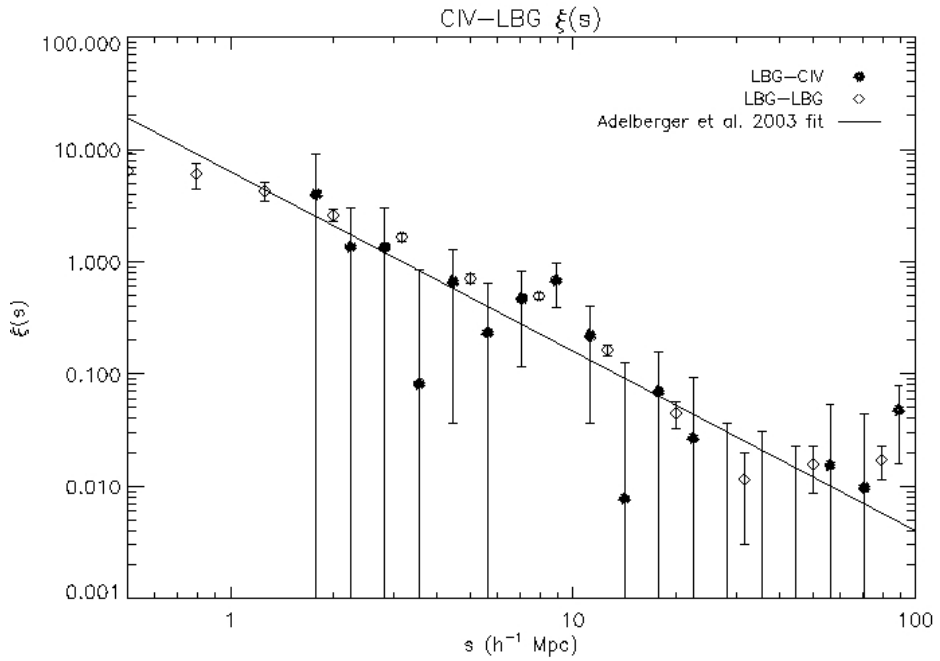

Figure 4.9: The comparison of CIV-LBG $\xi(s)$ and LBG-LBG $\xi(s)$, which are represented by filled circles and open diamonds respectively. The straight line is the power law fit to CIV-LBG correlation function by Adelberger et al. 2003, $\gamma = 1.60 \pm 0.20$ and $r_0 = 3.17 \pm 0.29$ Mpc.

The LBG $\xi(s)$ is from the combined data of Bielby et al. (2008) and Steidel et al. (2003). We see a similar trend between the auto-correlation function of galaxies with the cross-correlation function of galaxies with CIV systems. The results show strong clustering at small separations, although the errors are large for the CIV-LBG $\xi(s)$. Both appear to be power laws with agreement in fit parameters from Adelberger et al. 2003, $\gamma = 1.60 \pm 0.20$ and $r_0 = 3.17 \pm 0.29\ h^{-1}$ Mpc. The error bars are calculated from the Poisson estimate. The error bars in LBG-LBG $\xi(s)$ are smaller than in CIV-LBG $\xi(s)$ because of the large number of LBGs than CIV systems.

4.5 Conclusions

In this chapter, we used Lyα-LBG $\xi(s)$ to investigate the interaction between the IGM and galaxy at z $\sim$ 3. We calculated $\xi(s)$ from the LBGs and the transmissivity in Lyα forest from QSOs at high and low resolution spectra. All VLT data are obtained from Bielby et al. (2008). We use different approaches to reanalyze the Lyα-LBG $\xi(s)$ with different ways of estimating errors. Instead of using the Landy-Szalay estimator, we use the simpler form of $\xi(s) = \frac{<DT(s)>}{N(s)}$. We have tried three methods of error estimation as mentioned above and found that LBG-LBG error (method 3) seems to give the best errors particularly at small scales. Our results are similar to Bielby et al. (2008) but with slightly smaller error bars. Both results from high and low resolution spectra are compared to Adelberger et al. (2003) and Adelberger et al. (2005). At small separations ($s < 3h^{-1}$ Mpc), our results are in good agreement with Adelberger et al. (2003) which show a decrease in H_I density. However, our results have the same trend as Adelberger et al. (2003) and Adelberger et al. (2005) at larger scales, the transmissivity increases and reaches the mean value at $< flux/cont > \approx 0.65$. There is not much difference in $\xi(s)$ calculated from high and low resolution QSO spectra. The results at small scale are interesting since this lack of neutral Hydrogen at close distances to galaxies may imply the existence of winds from star forming galaxies. However, the number of LBGs

that contribute to small separations is still small. It is still difficult to state a definitive conclusion for the effect from winds. More observations and more data are needed.

We also looked at the connection between LBGs and CIV systems. By looking at CIV-LBG cross correlation and LBG-LBG correlation function, we see consistency from both results. Both are well fitted by the power law from Adelberger et al. 2003, $\gamma = 1.60 \pm 0.20$ and $r_0 = 3.17 \pm 0.29$ Mpc. This implies that the CIV systems and LBGs may be the same objects as they show the same clustering behaviour. As found by Adelberger et al. (2003), the metals in the QSO spectra may be closely connected to the star-forming galaxies themselves.

Chapter 5 | *Simulations*

We employed gas dynamical simulations to create both Lyα spectra and galaxies to compare the models with the data. Our main aims are therefore to study (a) the LBG-LBG $\xi(s)$ to see if we can detect the effects of peculiar velocities and possibly feedback by comparing real and redshift space correlation function, (b) the LBG-Lyα $\xi(s)$ to understand more about outflow and feedback.

5.1 GIMIC simulations

The Millennium simulation is one of the largest simulations that contains dark matter and was created by the Virgo consortium (Springel, 2005). It contains 10^{10} particles in a large cube of side, L = 500 h^{-1} Mpc. This simulation only considers the gravity from dark matter. However, at smaller scales the effects of baryons, such as feedback, will be important. Hydrodynamic simulations are introduced to resolve this problem. They include baryons and gas at small scales. The Galaxies-Intergalactic Medium Interaction Calculation (GIMIC) simulation combines the Millennium simulation of dark matter at large scales and hydrodynamic simulations of gas and baryons at small scales.

The idea of GIMIC is to select five regions of different density and then re-simulate the conditions and densities in the Millennium simulation. GIMIC selects some regions from the Millennium simulation, with either average, above or below average density. Then they go back to the original initial conditions for this simulation box and resimulate, adding many features such as star formation, gas cooling and photoionisation, chemical and winds feedback (Crain, 2009). This is done at high resolution in the re-simulation box whereas outside the box the simulation has lower resolution.

There are five density regions of radius 18 h^{-1} Mpc which each deviate from the cosmic mean in the GIMIC simulation, by -2σ, -1σ, 0σ, $+1\sigma$, and $+2\sigma$, where σ is the rms mass fluctuation on a scale of $\sim$ 20 h^{-1} Mpc. The simulation parameters are: Ω_m = 0.25, Ω_λ = 0.75, Ω_b = 0.045, H_0 = $100hkms^{-1}$ Mpc^{-1} and h = 0.73. The simulation contains many features such as star formation, gas cooling and photoionisation, chemical and winds feedback. The features of the simulations are summarized briefly below.

Star Formation

The relation between star formation rate and gas column density can be observed by studying nearby galaxies. When the density of gas particles is more than $n_H = 0.1cm^{-3}$, the star formation algorithm will assume that the gas particles are unstable and then convert them to stars. The equation of state $P \propto \rho_g^{\gamma_{eff}}$ with $\gamma_{eff} = 4/3$ is applied to these regions. This change of equation of state is to take into account SNe exploding which will add extra pressure to the gas. From the Kennicutt-Schmidt law (Kennicutt et al. 1998), gas particles are converted into stars if their surrounding gas density is high enough. The number of particles in the simulation is also converted by this means.

Gas cooling and photoionisation

The IGM is heated by a redshift dependent UV background from galaxies and quasars. In the simulation, they assumed hydrogen reionises at redshift z = 9, and Helium II reionises at redshift z = 3.5. The radiative cooling rates are computed on an element-by-element basis. By assuming the gas to be in ionisation equilibrium and optically thin, they used tables computed with CLOUDY (Ferland et al. 1998) to interpolate the cooling contribution of 11 elements: H, He, C, N, O, Ne, Mg, Si, S, Ca and, Fe, as a function of temperature, redshift, and gas density (Wiersma, 2009b). To calculate the cooling rate, all metals from CLOUDY are summed with the contributions from H, He, inverse Compton scattering and thermal Bremsstrahlung. During Hydrogen and Helium II reionisation, the ionisation is assumed to be balanced but the heating rate is increased to imitate non-equilibrium and radiative-transfer effects.

Chemical and winds feedback

From many observations (Heckman et al. 1990; Martin et al. 1999; Pettini et al. 2002; Adelberger et al. 2003; Shapley et al. 2003), feedback is believed to be the key factor of enriching the IGM with metals. Adelberger et al. (2003) suggested that feedback from supernovae disrupt the star formation. The simulation also includes the wind model. In this simulation, they assume a mass-loading of $\eta \equiv \dot{m_{wind}}/\dot{m_\star} = 4$ to recreate the peak in star formation rate and a wind speed of $\mathrm{v}_{wind} = 600\mathrm{kms}^{-1}$. They assume that this escaping wind can eject 80 per cent of heat from the supernova.

5.2 Galaxies from the simulation

The galaxies were made up from the particles that have been identified from the baryonic content of dark matter haloes. The Friends-of-Friends algorithm (FoF) (Davis et al. 1995; Lacey & Cole et al. 1994) is applied to group dark matter particles from the simulation (see Crain et al. 2009 for more details). In the simulation, they then employed the SUBFIND algorithm (Springel et al. 2001; Dolag et al. 2008) to identify a galaxy as the set of baryonic particles, ie. gas and stars.

Galaxies are found in an 18 h^{-1} Mpc radius simulation volume and are defined to have a stellar mass greater than $1 \times 10^9 h^{-1} M_\odot$ in each redshift snapshot. In this calculation, we get total 5931 galaxies from snapshot019 ($z = 3.06$) in the 0σ density region. The stellar mass is used to select the number of galaxies. We defined the LBGs by selecting at stellar mass greater than $5 \times 10^{10} h^{-1} M_\odot$ but we only get 7 LBGs. Then we consider smaller stellar mass to select the LBGs. We then use 4 sets of stellar mass which are greater than $5 \times 10^9 h^{-1} M_\odot$, $2 \times 10^9 h^{-1} M_\odot$, $0.9 \times 10^9 h^{-1} M_\odot$, and all stellar mass in the simulation. Finally we get 117, 235, 508, and 5931 LBGs or rather galaxies.

The effect of redshift distortion also affects this simulation as shown in Figure 5.1.

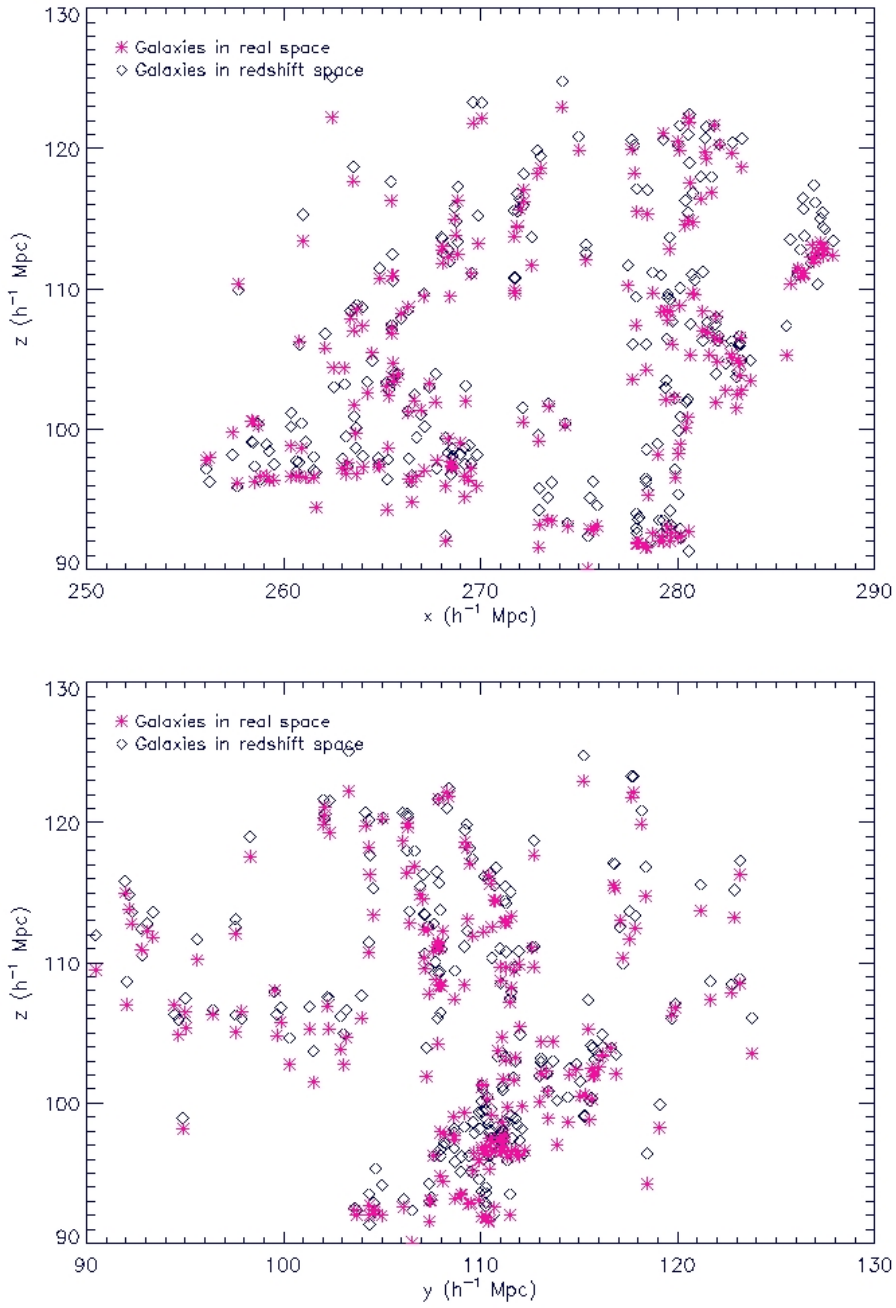

Figure 5.1: The position of galaxies at z = 3 in the x-z plane and y-z plane. The diamonds show the position of galaxies in redshift space while the pink asterisk illustrate galaxies in real space.

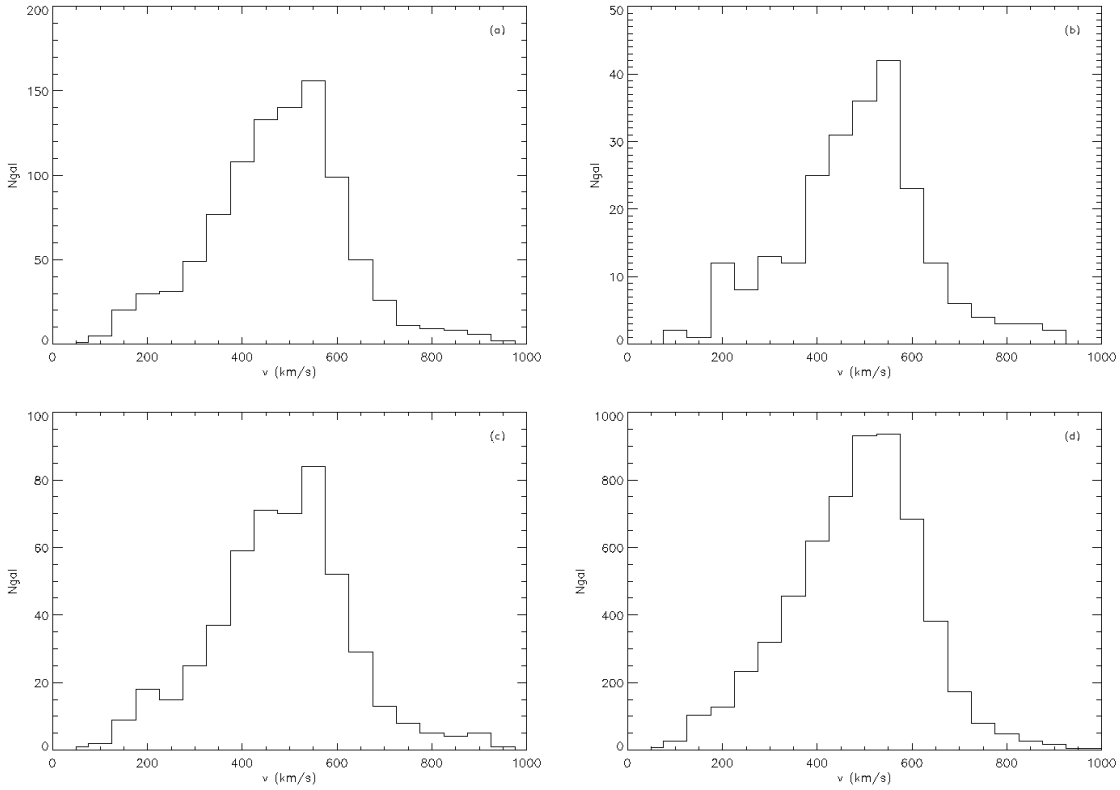

Figure 5.2: a (left-top), b (right-top), c (left-bottom), and d (right-bottom) show average velocity of galaxies from 117, 235, 508, and 5931 respectively. The average velocity are $456.33 \pm 67.70 kms^{-1}$, $457.19 \pm 94.23 kms^{-1}$, $456.75 \pm 134.77 kms^{-1}$, and $455.35 \pm 136.73 kms^{-1}$ respectively.

The diamonds show the position of galaxies in redshift space while the pink asterisks illustrate galaxies in real space. The peculiar velocity makes the galaxies in redshift space move to higher positions in z direction. This is because of bulk motion. The velocity distributions of galaxies are shown in Figure 5.2. The average velocities of v_x, x_y, v_z in x, y, z direction and standard deviation are 456.33 $\pm$ 67.70 kms^{-1}, 457.19 $\pm$ 94.23 kms^{-1}, 456.75 $\pm$ 134.77 kms^{-1}, and 455.35 $\pm$ 136.73 kms^{-1} for 117, 235, 508, and 5931 LBGs respectively.

5.3 Lyman alpha absorption lines

In order to calculate the galaxy-Lyα cross-correlation function, we use GIMIC to generate many sightlines in each snapshot. The sightlines were extracted by using SPECWIZARD programme performed by J. Schaye, C. Booth and T. Theuns (see Shone, 2009). There are many parameters in the SPECWIZARD programme such as the metallicity in the IGM, the scaling of the Haardt and Madau (2001) UV background, that need to be adjusted.

There are 11 elements; H, He, C, N, O, Ne, Mg, Si, S, Ca, Fe, that contribute in this code. We only use the absorptions from the Lyα transition of H I.

The number of sightlines: we need many sightlines to compare with the observations. The simulation can generate 675 sightlines in each redshift snapshot. Since the box size is not big, many sightlines may be oversampled. As a result, we use only 50 sightlines in our calculations. Figure 5.3 presents the position of random sightlines and galaxies in the x-y plane.

In the Lyα-LBG $\xi(s)$ calculation, we use the transmissivity of Lyα forest which are

$$T = \frac{f}{f_{con}} \tag{5.1}$$

where f is the measured flux and f_{con} is the continuum in flux level from Lyα forest.

Element	n_i/n_H	Mass Fraction
H	1	0.7065
He	0.1	0.2806
C	2.46×10^{-4}	2.07×10^{-3}
N	8.51×10^{-5}	8.36×10^{-4}
O	4.90×10^{-4}	5.49×10^{-3}
Ne	1.00×10^{-4}	1.41×10^{-3}
Mg	3.47×10^{-5}	5.91×10^{-4}
Si	3.47×10^{-5}	6.83×10^{-4}
S	1.86×10^{-5}	4.09×10^{-4}
Ca	2.29×10^{-6}	6.44×10^{-5}
Fe	2.82×10^{-5}	1.10×10^{-3}

Table 5.1: (from Wiersma 2009b): The contribution of 11 elements to the radiative cooling at T $> 10^4$.

The transmissivities from each sightline are shown in Figure 5.4.

5.4 LBG -LBG $\xi(s)$

We calculate $\xi(s)$ and $\xi(r)$ from galaxies in redshift and real space respectively. The correlation function was calculated at $z = 3.06$ at 0σ. We employed the estimation methods used in previous chapter.

$$\xi(s) = \frac{N_r < DD(s) >}{N_g < DR(s) >} - 1 \tag{5.2}$$

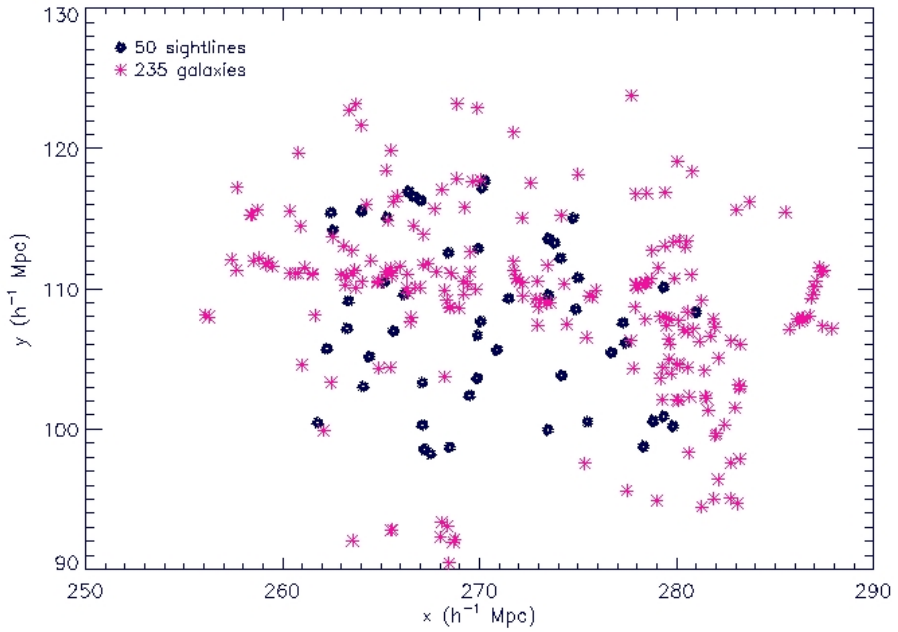

Figure 5.3: The position of random sightlines and galaxies in the x-y plane. The filled circles show the position of 50 sightlines while the pink asterisk illustrate galaxies.

where $< DD(s) >$ is the average number of LBG-LBG pairs. $< DR(s) >$ is the number of pairs of LBG-random LBGs at the separation s. The factor $\frac{Nr}{N_g}$ is the ratio of the number of random to data points. The errors are estimated by the Poisson error estimate as described in Chapter 3.

5.4.1 Result

Figure 5.5 shows the LBG-LBG correlation function from our simulations. The error bars are calculated by Poisson error estimate as mentioned in Chapter 3. The diamonds show LBG-LBG $\xi(s)$ results from galaxies in redshift space while the pink asterisks illustrate the results from galaxies in real space. The pink lines are roughly estimated power law

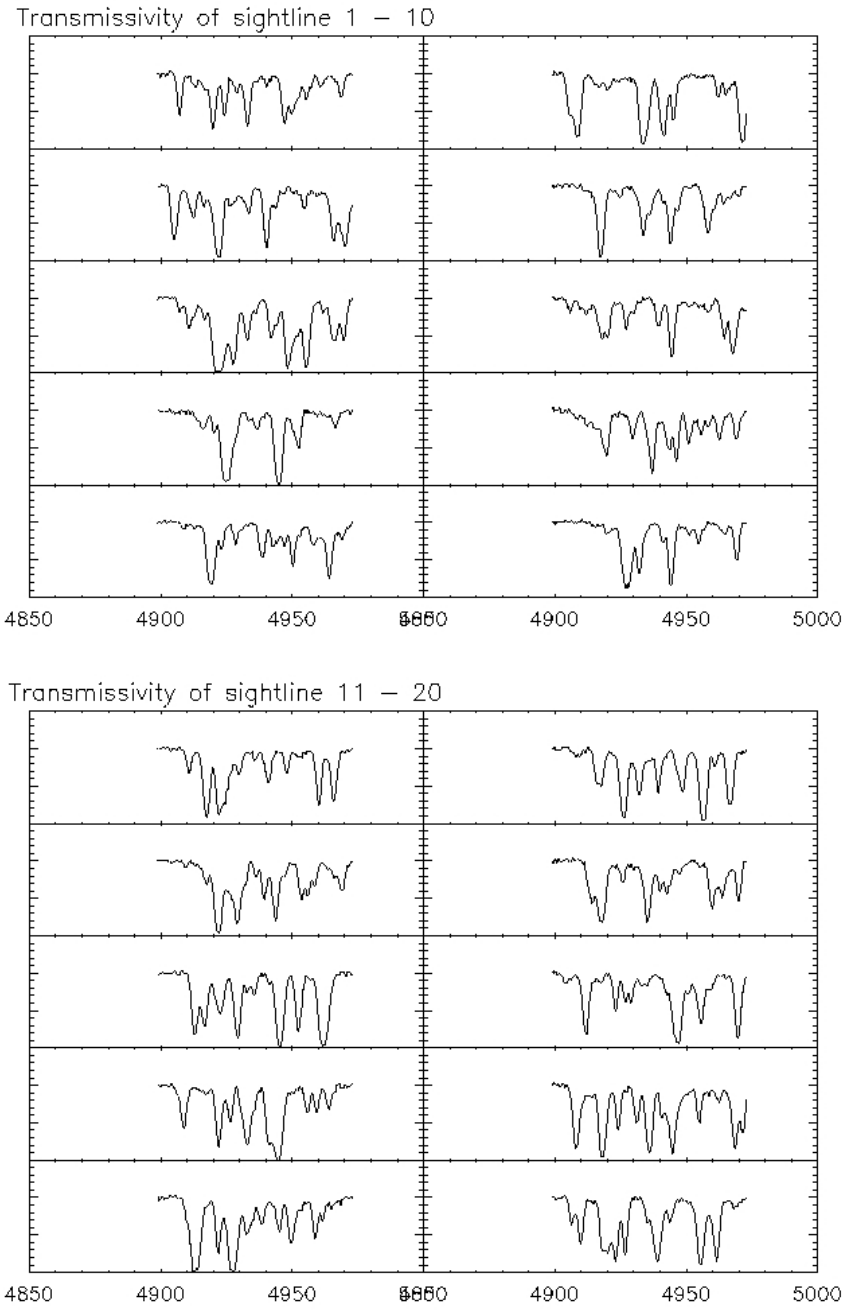

Figure 5.4: The transmissivity from each sightline.

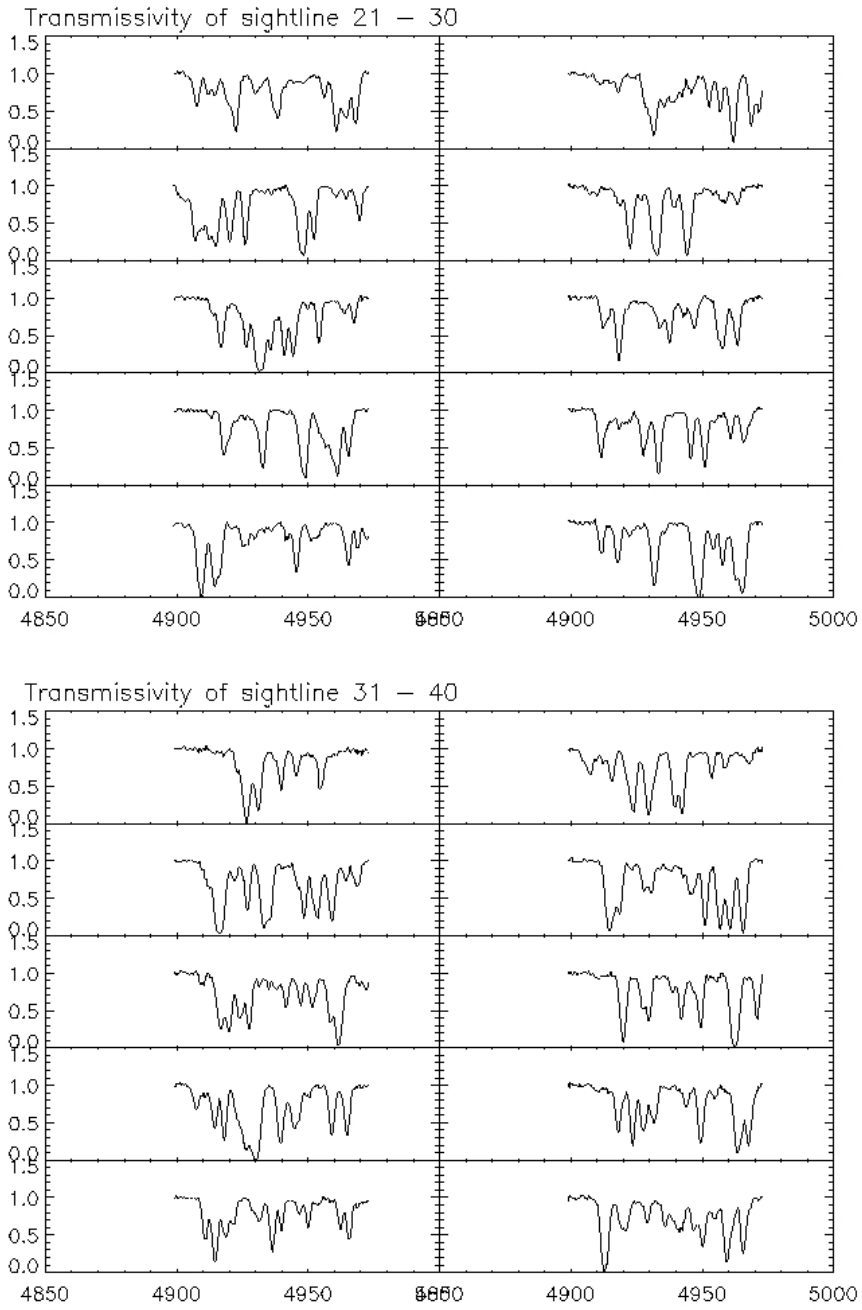

Figure 5.4: The transmissivity from each sightline.

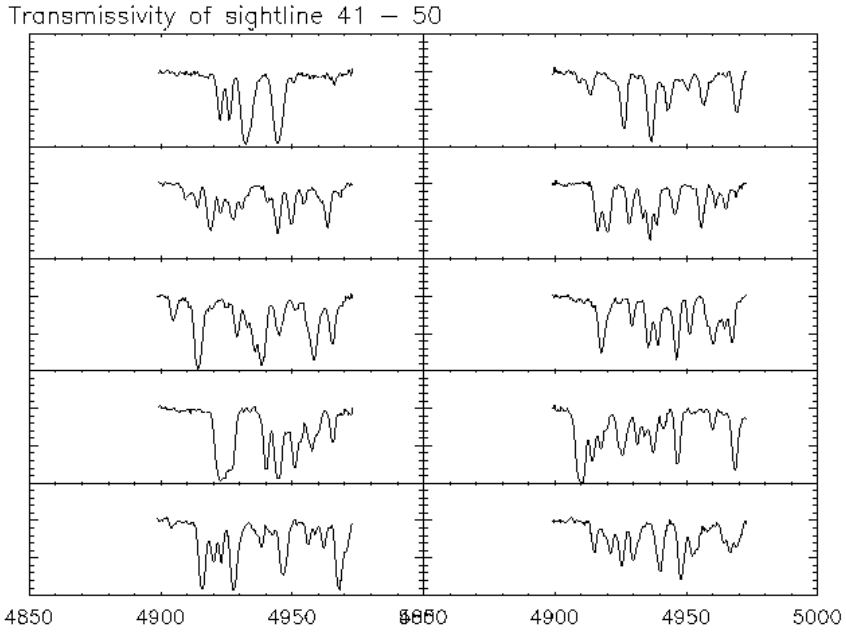

Figure 5.4: The transmissivity from each sightline.

Number of LBGs	r_0	γ	β	$< w_z^2 >^{\frac{1}{2}}$
117	4.2	2.1	0.15	55.27
235	4.0	2	0.17	76.91
508	3.9	1.8	0.14	110.06
5931	1.7	1.6	0.014	111.62

Table 5.2: Our $\xi(r)$, infall and pairwise velocity dispersion parameters to be used in the $z-$space distortions model from da Angela et al. (2005) for our Lyα-LBG $\xi(s)$ and $\xi(r)$ in Figure 5.5. $< w_z^2 >^{\frac{1}{2}}$ is the pairwise, 1-D velocity dispersion.

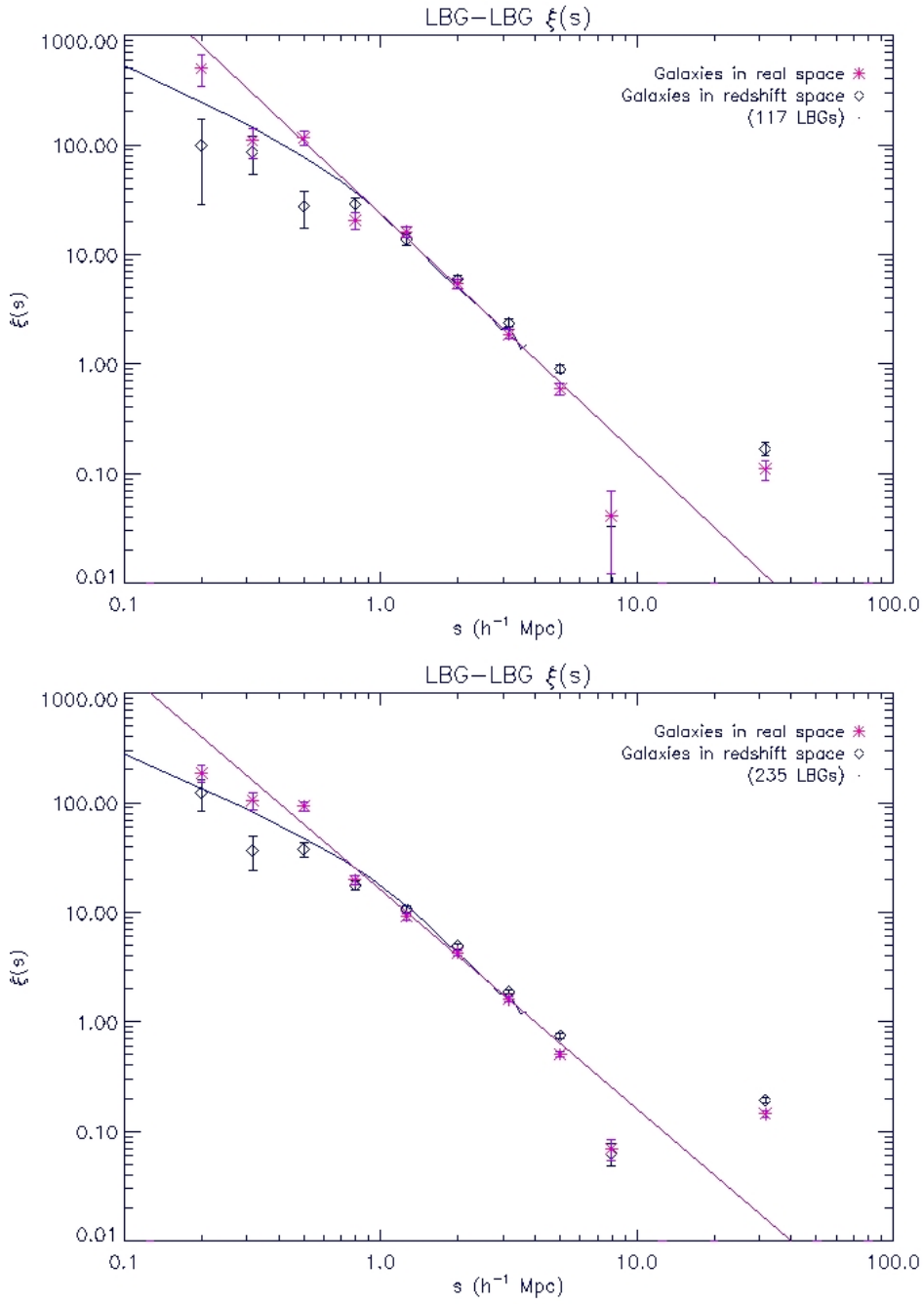

Figure 5.5: a (top) and b (bottom) show LBG-LBG $\xi(s)$ with 117 and 235 LBGs respectively. The diamonds show results from galaxies in redshift space while the pink asterisks illustrate the results from galaxies in real space. The pink lines are roughly estimate power law fit with a) $\gamma = 2.1$ and $r_0 = 4.2$ Mpc, b) $\gamma = 2.0$ and $r_0 = 4.0$ Mpc. The blue line is the fit from $z-$space distortions model from da Angela (2005) using our parameters from Table 5.2.

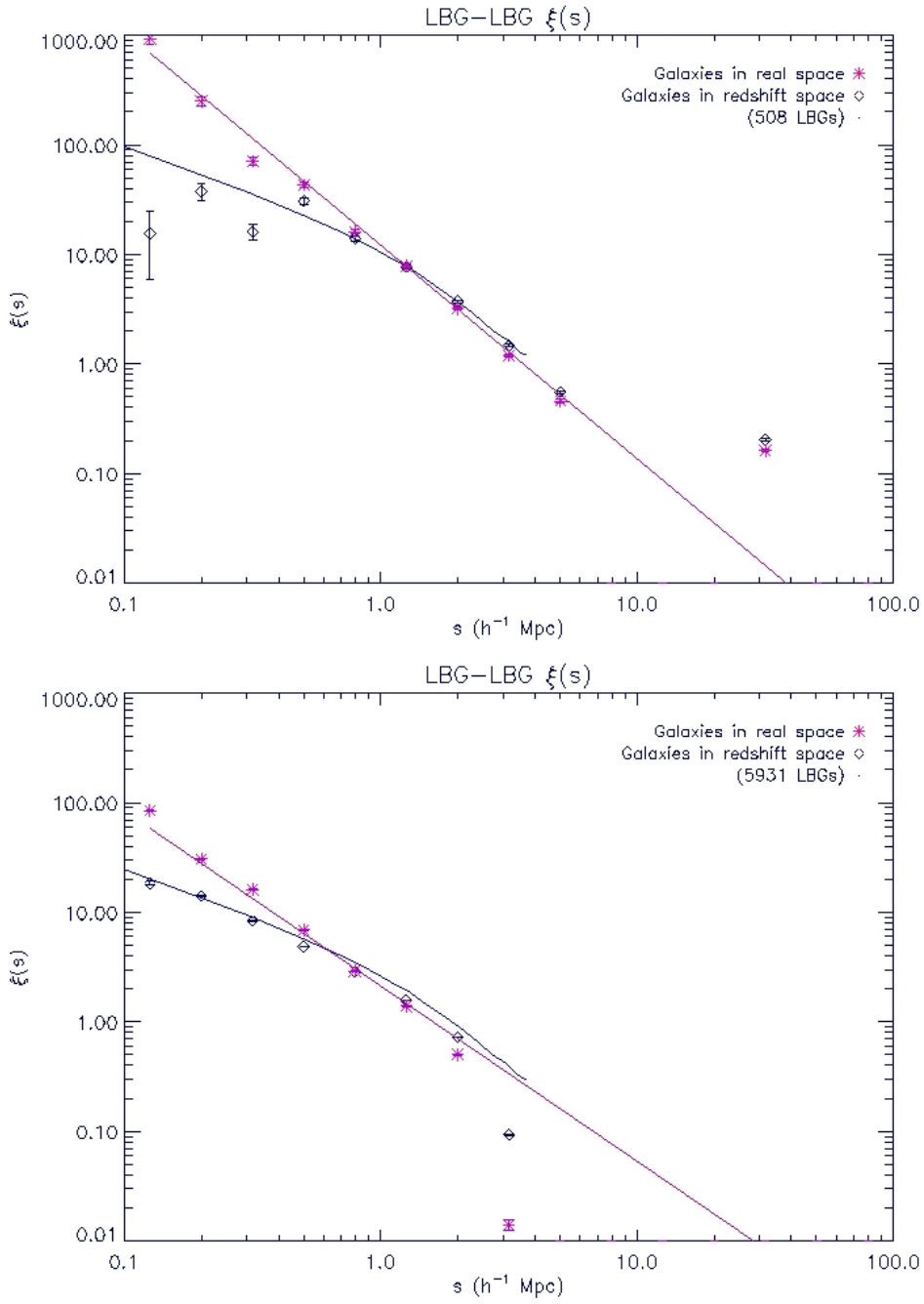

Figure 5.5: c (top) and d (bottom) show LBG-LBG $\xi(s)$ with 508 and 5931 LBGs respectively. The diamonds show results from galaxies in redshift space while the pink asterisks illustrate the results from galaxies in real space. The pink lines are roughly estimate power law fit with c) $\gamma = 1.8$ and $r_0 = 3.9$ Mpc, d) $\gamma = 1.6$ and $r_0 = 1.7$ Mpc. The blue line is the fit from $z-$space distortions model from da Angela (2005) using our parameters from Table 5.2.

fit with a) $\gamma = 2.1$ and $r_0 = 4.2$ Mpc, b) $\gamma = 2.0$ and $r_0 = 4.0$ Mpc, c) $\gamma = 1.8$ and $r_0 = 3.9$ Mpc, and d) $\gamma = 1.6$ and $r_0 = 1.7$ Mpc. The $< w_z^2 >^{\frac{1}{2}}$ and β are shown in Table 5.2. β comes from the rough estimate $\xi(s)/\xi(r)$ as calculated in Chapter 3. The blue lines are plotted by using our parameters for the $z-$space distortions model in da Angela et al. (2005).

In each plot, $\xi(r)$ in real space and $\xi(s)$ in redshift space show the same trend and tend to appear as a power law at large scales. At small separations ($s < 1h^{-1}Mpc$), the LBG-LBG $\xi(s)$ in redshift space have lower clustering than $\xi(r)$, while $\xi(s)$ at larger scales appears to have higher clustering. This may imply the main effect in redshift space that affects the clustering on small scales comes from the peculiar velocity dispersion $< w_z^2 >^{\frac{1}{2}}$. As described in Chapter 3, we used our parameters to the $z-$space distortions model from da Angela et al. (2005) to test the effects of peculiar velocities at small scales. Figure 5.5 shows that the $< w_z^2 >^{\frac{1}{2}}$ is consistent with $\xi(r)$ and $\xi(s)$.

5.5 Lyα-LBG $\xi(s)$

As discussed in Chapter 4, Lyα-LBG cross correlation function was evaluated from

$$\xi(s) = \frac{< DT(s) >}{N(s)} \tag{5.3}$$

where $< DT(s) >$ is the number of galaxy-Lyα pairs weighted by the transmissivity: T for each separation. N(s) is the number of LBGs that contribute in each pairs. The LBG-LBG error estimate as described in Chapter 4 was used in this calculation.

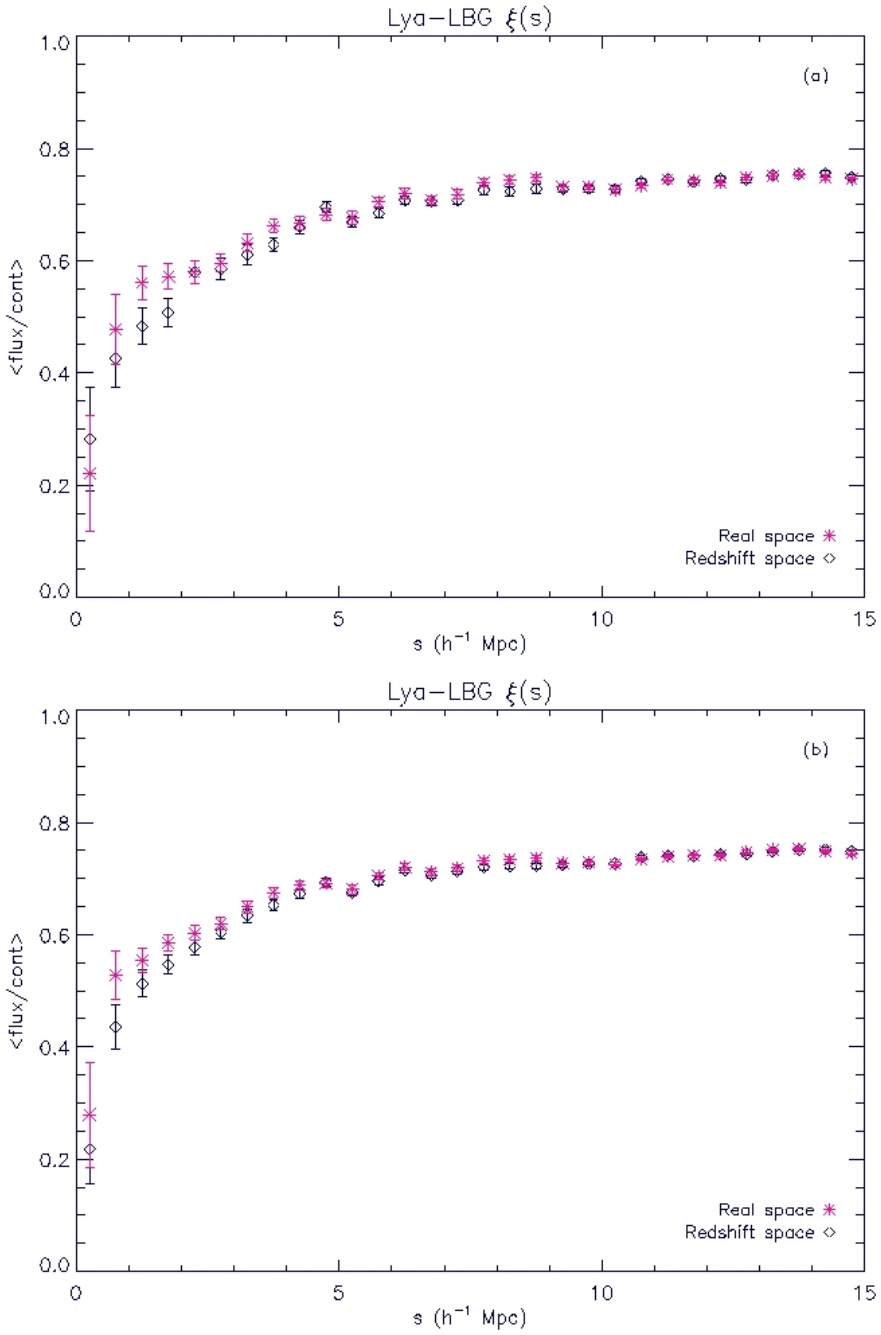

Figure 5.6: a (top) and b (bottom) show Lyα-LBGs $\xi(s)$ from LBG in real space (pink asterisks) vs LBG in $z-$space (open diamonds) with 117 and 235 LBGs respectively.

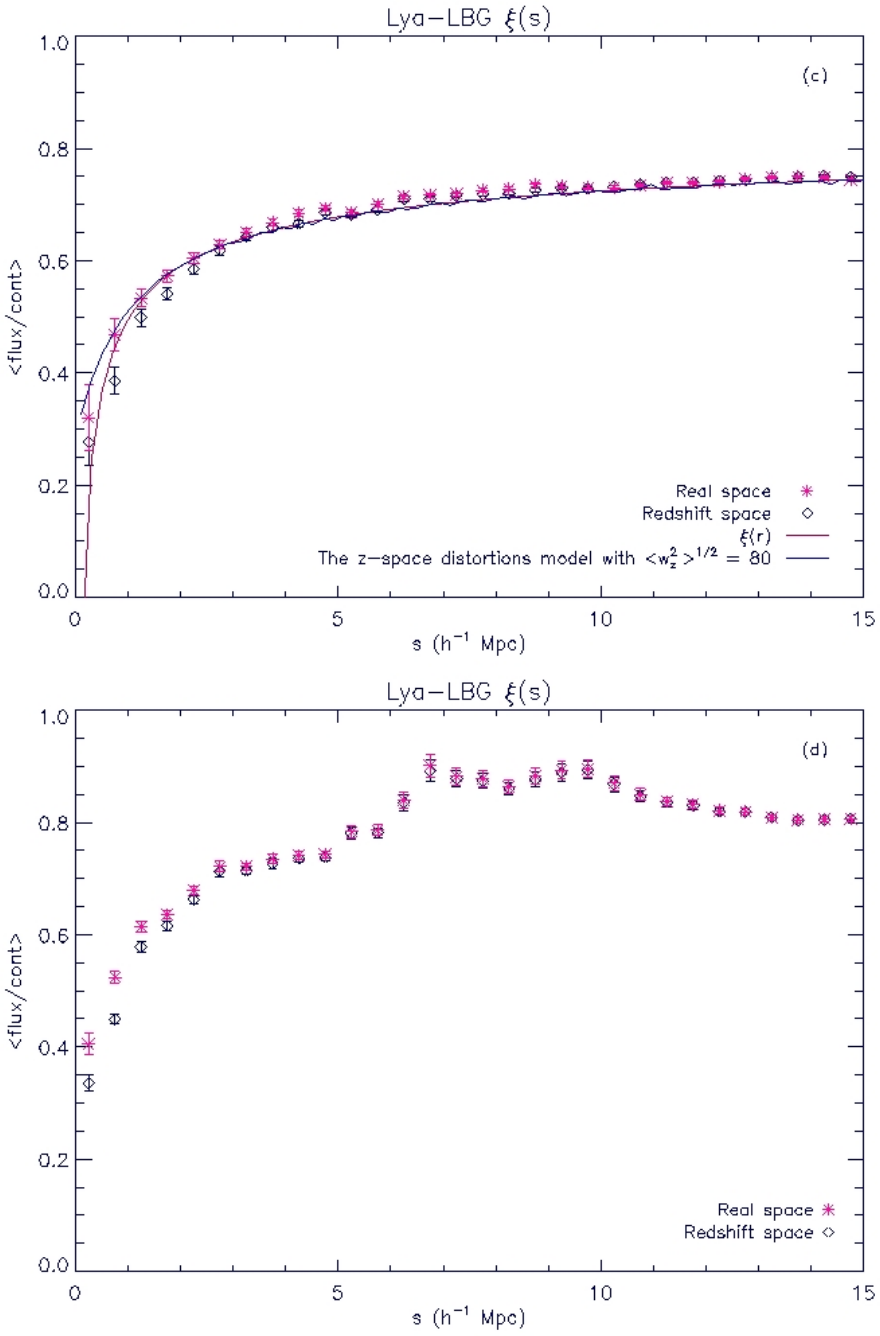

Figure 5.6: c (top) and d (bottom) show Lyα-LBGs $\xi(s)$ from LBG in real space (pink asterisks) vs LBG in $z-$space (open diamonds) with 508 and 5931 LBGs respectively. In top panel, we fitted $\xi(r)$ (the pink line) by $\gamma = 0.45$ and $r_0 = 0.1h^{-1}$ Mpc. The blue solid line is the $z-$space distortions model from da Angela et al. (2005), here assuming $\gamma = 0.45$, $r_0 = 0.1h^{-1}$ Mpc, $\beta = 0.2$, and $< w_z^2 >^{\frac{1}{2}} = 80 kms^{-1}$.

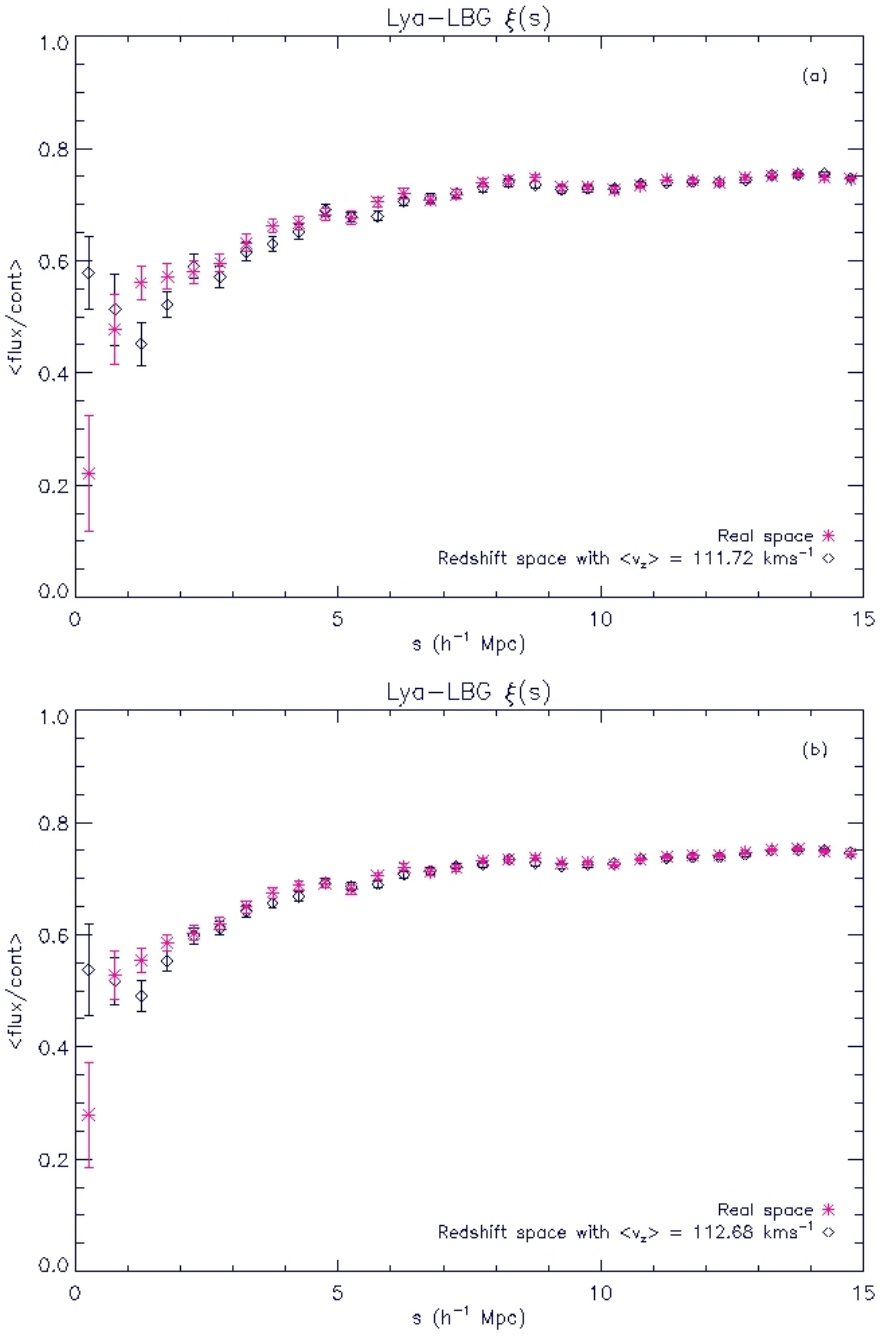

Figure 5.7: a (top) and b (bottom) show Lyα-LBGs $\xi(s)$ from LBG in real space (pink asterisks) vs LBG in $z-$space (open diamonds) with 117 and 235 LBGs respectively. We added $< v_z > = 111.72\ kms^{-1}$ and $112.68\ kms^{-1}$ to the galaxies (open diamonds) in (a) and (b) respectively.

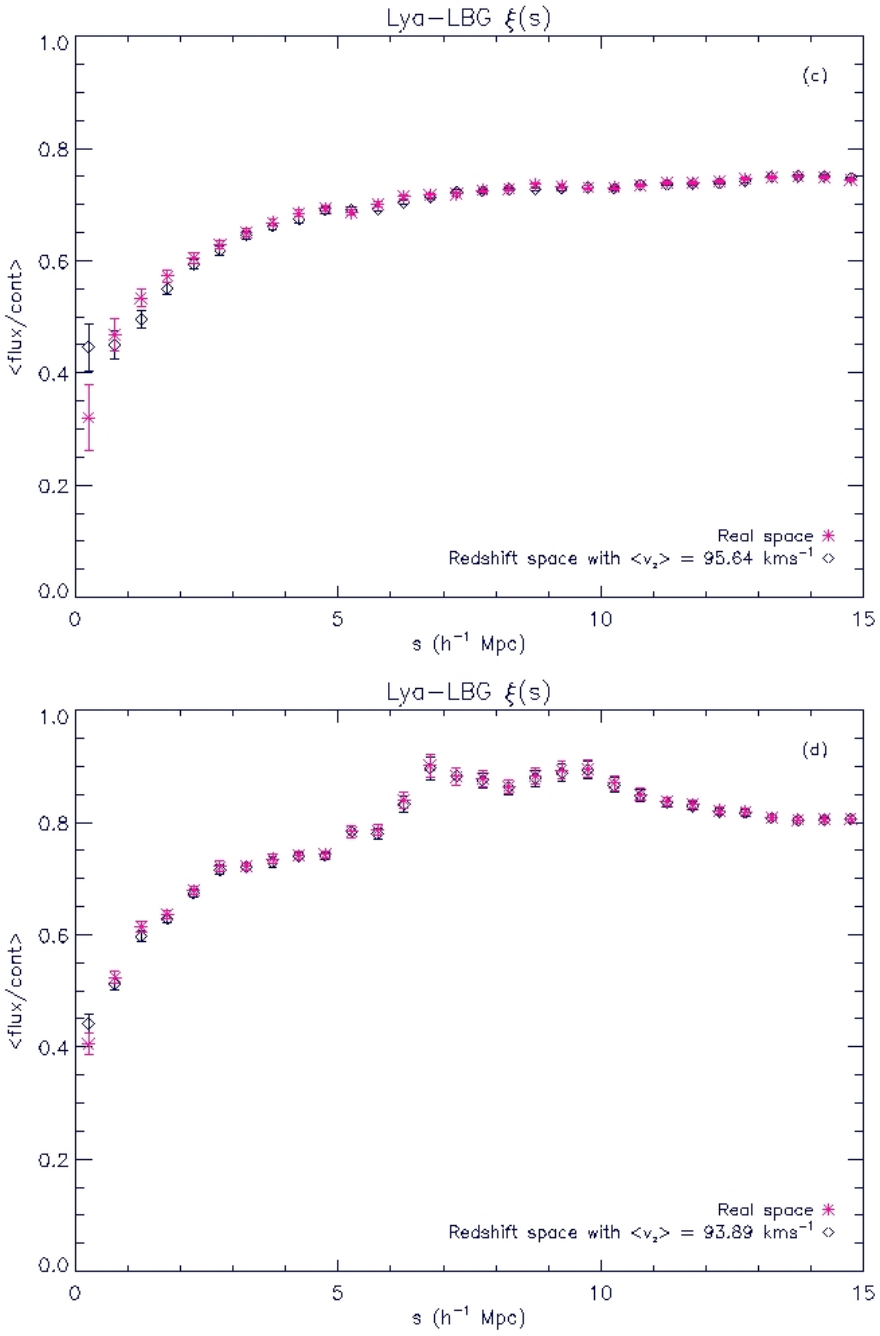

Figure 5.7: c (top) and d (bottom) show Lyα-LBGs $\xi(s)$ from LBG in in real space (pink asterisks) vs LBG in $z-$space (open diamonds) with 508 and 5931 LBGs respectively. We added $< v_z > = 95.64\ kms^{-1}$ and $93.89\ kms^{-1}$ to the galaxies (open diamonds) in (c) and (d) respectively.

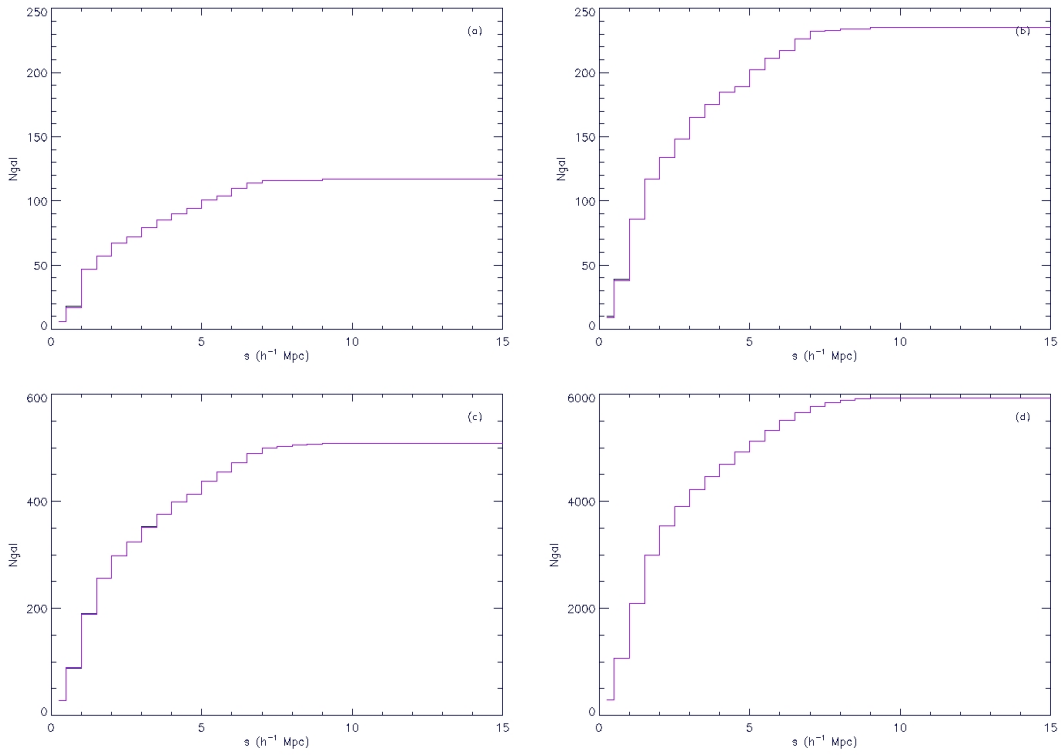

Figure 5.8: a (left-top), b (right-top), c (left-bottom), and d (right-bottom) show the number of LBGs in each separation which contribute to the Lyα-LBGs $\xi(s)$ calculated from 117, 235, 508, and 5931 LBGs respectively.

5.5.1 Result

Figure 5.6 presents the LBG-Lyα transmissivity correlation function from the galaxies in real vs redshift space. The open diamonds show the results from galaxies in redshift space while the pink asterisks illustrate the results from galaxies in real space. The lyα forest only has redshift space for both the diamonds and the asterisks. Our bin size is 0.5 h^{-1} Mpc. Both results show the same trend. At a distance greater than 5 h^{-1} Mpc, the measured $< flux/cont >$ increases and reaches the mean value at $< flux/cont > \approx 0.70$. At separation decrease below 5 h^{-1} Mpc, we found a decrease in H_I density. However, it still hard to see the effect of the wind from the simulation.

Considering the effect of LBGs in real vs redshift space, we can see that in redshift space $< flux/cont >$ decreases at separations 5 h^{-1} Mpc. When we added $< v_z >$ in real space, r, for the galaxies, we retrieved the same result as in Figure 5.6. In Figure 5.7 (a) - (c) , at the separations less than $5h^{-1}$ Mpc, LBG-Lyα $\xi(s)$ in redshift space (open diamonds) $< flux/cont >$ is smaller than in real space (pink asterisks) but then higher at the small separations, $s < 2h^{-1}$ Mpc. This is due to the small number of LBGs at the small separations. However we see the same result of LBG-Lyα $\xi(s)$ in real space vs $z-$space in Figure 5.7 (d). The similar results in Figure 5.6 and Figure 5.7 means that the dominant effect in producing the different $z-$space result is in the bulk motions. Therefore, we have not detected the effect of random peculiar velocities and winds in these analyses of the simulations. The number of LBGs that contribute to each bin are presented in Figure 5.8. The effect of LBG peculiar velocities is not expected to be large. Table 5.2 gives $< w_z^2 >^{\frac{1}{2}} = 111.62 kms^{-1}$ as the maximum velocity dispersion. This corrects to $\frac{\sqrt{2} \times 136.70}{\sqrt{3}} = 111.62 kms^{-1}$ which corresponds to $0.8h^{-1}$ Mpc (comoving) at $z = 3$. The effect of adding this error into LBG-Lyα $\xi(s)$ in Figure 5.6 will be negligible at most separations. This is confirmed by Figure 5.6 (c) where we compare the result of smoothing real-space model by the peculiar velocity calculated from Table 5.2. The two results are very similar due to the low intrinsic velocity dispersion (compared to Figure

4.6 (a)).

5.6 Conclusions

We employed the GIMIC simulations to create synthetic Lyα spectra and galaxies. We calculated the LBG-LBG $\xi(s)$ and LBG-Lyα $\xi(s)$ to check the feedback of real vs z-space at redshift $z \sim 3$. For LBG-LBG $\xi(s)$, we used different number of galaxies, 117, 235, 508, and 5931 which are selected by their stellar mass. The LBG-LBG $\xi(r)$ and $\xi(s)$ in real and redshift space appear to be power laws at large scales. They show strong clustering at small separations. At small distances ($s < 1h^{-1}$ Mpc), the LBG-LBG $\xi(s)$ in redshift space tend to have lower clustering than $\xi(r)$ in real space, while at larger scales the LBG-LBG $\xi(s)$ results appear to have higher clustering. This may imply the main effect in redshift space that affects the clustering on small scales from peculiar velocity $< w_z^2 >^{\frac{1}{2}}$. Figure 5.5 shows that the measured $< w_z^2 >^{\frac{1}{2}}$ can explain the form of $\xi(s)$ based on the measured $\xi(r)$.

We then measured the LBG-Lyα $\xi(s)$ to study the theoretical relationship between galaxies and the IGM at $z \sim 3$. The LBG-Lyα $\xi(s)$ is also computed with different number of galaxies (117, 235, 508, and 5931 LBGs). From simulation results, we found a decrease in $< flux/cont >$ at separation decrease below 5 h^{-1} Mpc but at the larger distance ($s > 5h^{-1}$ Mpc), the measured $< flux/cont >$ increases and reaches the mean value at $< flux/cont > \approx 0.70$. At small distances near the LBG, we see no effect of the wind from simulations. The results seem to agree with Adelberger et al. (2005) rather than Adelberger et al. (2003). Therefore they are less in agreement with our VLT results which shows some tentative evidence for feedback at small scales.

Chapter 6 | *Conclusions*

The interaction between galaxies and the IGM at z $\sim$ 3 is the main question addressed by this research. By using the cross-correlation function between galaxies and the Lyα forest in QSO sight-lines, we can analyze the relationship between galaxies and the IGM at $z \sim 3$. We have used LBG samples and the Lyα forest in QSO sight-lines supplied by the Bielby et al. (2008) VLT observations. The LBG redshifts have been measured in the fields of bright $z > 3$ QSOs from the UVES, Keck and SDSS. Additional QSO data are also available from the AAT AAOmega spectrograph at lower resolution. The low-resolution spectra are measured from fainter QSOs at z > 2. In total, we have 6 high-resolution QSO spectra and 22 low-resolution spectra. The total number of LBGs from VLT data is 1109 LBGs at $2 < z < 3.5$. We also included 813 LBGs at redshift $2.67 \leq z \leq 3.25$ from the Steidel et al. (2003) Keck samples.

We have measured the LBG-LBG correlation functions by using LBG data from VLT and Keck. Considering $\xi(s)$ from VLT data only, we see consistency between our result and that of Bielby et al. (2008). We have used some updated redshift estimates and this might cause the lower clustering at distances below $8h^{-1}$ Mpc compared to Bielby et al. (2008). We then compared the LBG-LBG $\xi(s)$ from Keck data with the $\xi(s)$ fit from da Angela et al. 2005 who used the Steidel et al. (2003) LBG samples. We see lower clustering at distances below $3h^{-1}$ Mpc but higher clustering at distances $> 3h^{-1}$ Mpc. This difference is possibly caused by the estimator that we used to calculate $\xi(s)$. We use the simple form of estimator, $\xi(s) = \frac{Nr}{Ng}\frac{<DD(s)>}{<DR(s)>} - 1$, while da Angela et al. (2005) used the Landy-Szalay estimator. Finally, we compared our VLT result with the Keck result. We see lower clustering from the VLT sample at scales $< 10h^{-1}$ Mpc. The error bars from VLT results are higher than in Keck. It is possible that our higher redshift errors

may make this difference.

We tested the effect of redshift errors by using the $z-$space distortions model from da Angela et al. (2005) by assuming $\gamma = 1.8$, $r_0 = 3.63h^{-1}$ Mpc, $\beta = 0.2$, and $< w_z^2 >^{\frac{1}{2}} = 650kms^{-1}$ for the VLT data. We used $\gamma = 1.76$, $r_0 = 4.48h^{-1}$ Mpc, $\beta = 0.25$, and $< w_z^2 >^{\frac{1}{2}} = 530kms^{-1}$ for the Keck data. Then we used the combined data from VLT and Keck to calculate LBG-LBG $\xi(s)$. The result from the combined data is consistent with the $\xi(s)$ from da Angela et al. (2005), where $\gamma = 1.71$ and $s_0 = 5.1$ h^{-1} Mpc. We also used the $z-$space distortions model to the combined data by assuming $\gamma = 1.8$, $r_0 = 3.63h^{-1}$ Mpc, $\beta = 0.2$, and $< w_z^2 >^{\frac{1}{2}} = 590kms^{-1}$. Comparing the VLT and the combined data cases, we see less effects of the peculiar velocity in the combined data. This is because of the better redshift estimation in Steidel et al. (2003). We also estimated the infall parameter, β at $z = 3$ by using the power-law $\xi(r)$ fitted from combined $w_p(\sigma)$ of Bielby et al. (2008) and the $\xi(s)$ measurements from the combined LBG data. By computing and fitting $\xi(s)/\xi(r)$, we get $\beta = 0.14^{+0.09}_{-0.05}$, at $z = 3$ which gives the LBG bias factor $b = 6.8$. This result agrees with Bielby et al. (2008) who get $\beta = 0.21^{+0.13}_{-0.12}$ which was estimated by fitting the power-law $\xi(r)$ to the measurement of $\xi(\sigma, \pi)$.

We calculated Lyα-LBG $\xi(s)$ and compared our results with Bielby et al. (2008) by using different approaches. Instead of using the Landy-Szalay estimator, we use the simple form of $\xi(s) = \frac{<DT(s)>}{N(s)}$. We have tried three methods of error estimation and found that LBG-LBG error seems to give the best errors particularly at small scales. Our results are similar to Bielby et al. (2008) but with slightly smaller error bars. Both results from high and low resolution spectra are compared to Adelberger et al. (2003) and Adelberger et al. (2005). At distances $s < 3h^{-1}$ Mpc, our results are in good agreement with Adelberger et al. (2003) which show a decrease in H_I density. However, our results have the same trend with Adelberger et al. (2003) and Adelberger et al. (2005) at larger scale, the transmissivity increases and reaches the mean value at $< flux/cont > \approx 0.65$. There are not much differences in $\xi(s)$ calculated from high and low resolution QSO

spectra. The results at small scale are interesting since this lack of neutral Hydrogen at their close distances to galaxies may imply the existence of winds from star forming galaxies. However, the number of LBGs that contribute to small separations is still small. It is still difficult to state the conclusion for the effect from winds. We also looked at the connection between LBGs and CIV systems. We see consistency from CIV-LBG and LBG-LBG correlation function. Both are well fitted by the power law from Adelberger et al. 2003, $\gamma = 1.60 \pm 0.20$ and $r_0 = 3.17 \pm 0.29$ Mpc. This implies that CIV systems and LBGs may be the same objects as they show the same clustering behaviour.

We then employed the GIMIC simulations to create Lyα spectra and galaxies. We calculated LBG-LBG $\xi(s)$ and LBG-Lyα $\xi(s)$ to check the feedback of real vs z-space at redshift $z \sim 3$. For LBG-LBG $\xi(s)$, we used different number of galaxies, 117, 235, 508, and 5931 which are selected by their stellar mass. $\xi(r)$ in real and $\xi(s)$ in redshift space appear to be power laws at large scale. They show strong clustering at small separations. At small distances ($s < 1h^{-1}$ Mpc), the LBG-LBG $\xi(s)$ in redshift space tends to have lower clustering than $\xi(r)$ in real space, while the larger scales the LBG-LBG $\xi(s)$ results appear to have higher clustering. This may imply the main effect in redshift space that affects the clustering on small scales from peculiar velocity $< w_z^2 >^{\frac{1}{2}}$. Our result shows that the $< w_z^2 >^{\frac{1}{2}}$ is consistent between $\xi(r)$ and $\xi(s)$.

The LBG-Lyα $\xi(s)$ are also computed with different number of galaxies. From simulation results, we found a decrease in $< flux/cont >$ at separation decrease below 5 h^{-1} Mpc. But at the larger distance ($s > 5h^{-1}$ Mpc), the measured $< flux/cont >$ is increased and reached the mean value at $< flux/cont > \approx 0.70$. At small distances near LBGs, we see no effect from the wind from simulations. The results seem to agree with Adelberger et al. (2005) rather than Adelberger et al. (2003). Therefore they are less in agreement with our VLT results which show some evidence for feedback at small scales.

The evidence of the existence of super-winds, supernovae driven winds at high-redshift can be shown by many observations (Heckman et al. 1990; Martin 1999; Pettini et al.

2002; Adelberger et al. 2003; Shapley et al. 2003). The properties of high-redshift outflows such as the size scale over which absorbing clouds are distributed, mass and energy outflow rates, driving mechanism, conserved quantities and fate of the outflowing material are still poor (Shapley, 2003). As mentioned above, most of our results (LBG-LBG and LBG-CIV correlation function) show consistency with da Angela et al. (2005) and Bielby et al. (2008). Although our Lyα-LBG $\xi(s)$ agrees with Adelberger et al. (2003), it shows disagreement with Adelberger et al. (2005) and the simulations. It is still hard to decide whether the winds have effects on the galaxy and its surroundings or not since we have small only a number of galaxies in this analysis. In order to understand properly the effect of feedback, the observations from more LBG-QSO fields and more QSOs with high S/N moderate resolution spectra are needed.

Bibliography

[1] Adelberger K. L., Steidel C. C., Shapley A. E. & Pettini M. 2003, ApJ, 584, 45

[2] Adelberger K. L., Shapley A. E., Steidel C. C., Pettini M., Erb D. K., & Reddy N. A. 2005, ApJ, 629, 636

[3] Bielby R. 2008, *Galaxy Clustering And Feedback*, PhD thesis

[4] Crain R. A., Theuns T., Vecchia C. D., Eke V. R., Frenk C. S., Jenkins A., Kay S. T., Peacock J. A., Pearce R., Schaye J., Springel V., Tomas P.A., White S. M. & Wiersma R. 2009, MNRAS, 000, 1-23

[5] da Angela J. 2005, *Clustering And Redshift − space Distortions in QSO and Galaxy Surveys*, PhD thesis

[6] Desjacques V., Haehnelt M.G. & Nusser A. 2006, MNRAS, 367, L74

[7] Ferland G. J., Korista K.T., Verner D.A., Ferguson J. W., Kingdon J.B. & Verner E.M. 1998, PASP, 110, 761

[8] Guzzo L., Strauss M.A., Fisher K.B., Giovanelli R. & Haynes M. P. 1997, ApJ, 489, 37-48

[9] Harrison E. R., 1970, PhRevD, 1, 2726

[10] Heckman T. M., Armus L., & Miley G. K. 1990, ApJS, 74, 833

[11] Jones A.W. & Lansenby A. N. 1998, *Living Reviews in Relativity*, 1

[12] Kawata D. & Rauch M. 2007, ApJ, 663, 38

[13] Keiser N. 1987, MNRAS, 227, 1-21

[14] Kollmeier J. A. & Miralda-Escude J. 2006, ApJ, 638, 52

[15] Lee T.S., Nagamine K., Hernquist L. & Springel V. 2007, MNRAS, 000, 1-10

[16] Liddle A. 2007, *An Introduction to Modern Cosmology*

[17] Magira H., Jing Y. P., & Suto Y. 2000, ApJ, 528

[18] Marble A.R., Eriksen K.A., Impey C.D., Oppenheimer B.D. & Dave R. 2008, ApJ, 675, 946

[19] Martin C. L. 1999, ApJ, 513, 156

[20] Nagamine K., Ouchi M., Springel V. & Hernquist L. 2008, ApJ

[21] Nilsson K.K. 2007, *The Lyα Emission Line as a Cosmology Tool*, PhD thesis

[22] Peebles P. J. E. & Yu J. T., 1970, ApJ, 162, 815

[23] Pettini M., Steidel C. C., Adelberger K. L., Dickinson M., Erb D. K. Giavalisco M., Law D. R., Reddy N. A. & Shapley A. E., 2007, IL NUOVO CIMENTO, 122, N9-11

[24] Pettini M., Rix S. A., Steidel C. C., Adelberger K. L., Hunt M. P. & Shapley A. E., 2002, ApJ, 569, 742

[25] Schaye J., Theuns T., Rauch M., Efstathiou G. & Sargent W. L. W., 2000, MNRAS, 318, 817

[26] Schneider P. 2006, *Extragalactic Astronomy and Cosmology*

[27] Shapley A. E., Steidel C. C., Pettini M. & Adelberger K. L., 2003, ApJ, 588, 65

[28] Shone A. M. 2009, *The Relationship Between Gas and Galaxy*, PhD thesis

[29] Steidel C. C., Adelberger K. L., Shapley A. E., Pettini M., Dickinson M. & Giavalisco M. 2003, ApJ, 592, 728

[30] Theuns T., Viel M., Kay S., Schaye J., Carswell R. F., & Tzanavaris P. 2002, MNRAS, 578, 5

[31] Wiersma R.P.C., Schaye J., Theuns T & Vecchia C.D. 2009, MNRAS, 000, 000

[32] Zel'Dovich Y. B., 1970, A&A, 5, 84

[33] Zhan H. & Fang L. 2002, ApJ, 566, 9